Distribution of slip from 11 M_w > 6 earthquakes in the northern Chile subduction zone

M. E. Pritchard,[1] C. Ji,[2,3] and M. Simons[2]

[1] We use interferometric synthetic aperture radar, GPS, and teleseismic data to constrain the relative location of coseismic slip from 11 earthquakes on the subduction interface in northern Chile (23°–25°S) between the years 1993 and 2000. We invert body wave waveforms and geodetic data both jointly and separately for the four largest earthquakes during this time period (1993 M_w 6.8; 1995 M_w 8.1; 1996 M_w 6.7; 1998 M_w 7.1). While the location of slip in the teleseismic-only, geodetic-only, and joint slip inversions is similar for the small earthquakes, there are differences for the 1995 M_w 8.1 event, probably related to nonuniqueness of models that fit the teleseismic data. There is a consistent mislocation of the Harvard centroid moment tensor locations of many of the $6 < M_w < 8$ earthquakes by 30–50 km toward the trench. For all models, the teleseismic data are better able to resolve fine details of the earthquake slip distribution. The 1995 earthquake did not rupture to the maximum depth of the seismogenic zone (as defined by the other earthquakes). In addition to the above events, we use only teleseismic data to determine the rupture characteristics of four other M_w > 6 earthquakes, as well as three M_w > 7 events from the 1980s. All of these earthquakes appear to rupture different portions of the fault interface and do not rerupture a limited number of asperities.

1. Introduction

[2] A principle goal of both teleseismic and geodetic studies of earthquakes is to resolve the spatial distribution of fault slip. Both geodetic and teleseismic data are non-unique: multiple slip distributions on a fault interface can explain either data set. We use both teleseismic and geodetic data to study four large earthquakes ($6.5 < M_w < 8.1$) in the northern Chile subduction zone. The complimentary nature of these data sets allows us to tightly constrain the distribution of slip, while exploring the relative contributions of each data set.

[3] We specifically focus on the following earthquakes: M_w 6.8, 11 July 1993; M_w 8.1, 30 July 1995; M_w 6.7, 19 April 1996; and M_w 7.1, 30 January 1998 (hereafter referred to as the 1993, 1995, 1996, and 1998 earthquakes (Figure 1)). In addition, we compare the inferred slip from these four events with three other M_w > 7 earthquakes from the same area that occurred during the late 1980s (before the advent of interferometric synthetic aperture radar (InSAR)), three M_w > 6 aftershocks of the 1995 earthquake that occurred within a few days of the 1995 main shock, and a M_w 6.4 event on 8 January 2000.

[4] The 1995 earthquake has been the subject of many investigations [*Campos et al.*, 1995; *Ruegg et al.*, 1996; *Ortlieb et al.*, 1996; *Delouis et al.*, 1997; *Ihmlé and Ruegg*, 1997; *Carlo et al.*, 1999; *Klotz et al.*, 1999; *Pritchard et al.*, 2002; *Xia et al.*, 2003]. However, a model of fault slip that describes teleseismic, GPS and InSAR data together is needed, because slip maps that used only teleseismic data, or teleseismic data and sparse geodesy are not consistent with the InSAR observations [*Pritchard et al.*, 2002]. The other earthquakes have not been previously studied. Constraining the spatiotemporal evolution of slip from all of these earthquakes is the first step to better understanding any causal connection between earthquakes or between earthquakes and aseismic slip.

2. Data Used

[5] Northern Chile is ideal for the use of satellite based InSAR because of the aridity of the region and the minimal amount of vegetation and human cultivation [e.g., *Pritchard and Simons*, 2004]. This area of South America is one of the few subduction zones were InSAR observations of large earthquakes are possible with existing data sets. In addition, there are both campaign and continuous GPS measurements from the SAGA and French-Chilean arrays [*Ruegg et al.*, 1996; *Klotz et al.*, 1999; *Chlieh et al.*, 2004] that provide independent constraints on the surface deformation from earthquakes during the period of interest. Even though there

---

[1] Department of Earth and Atmospheric Sciences, Cornell University, Ithaca, New York, USA.
[2] Seismological Laboratory, Division of Geological and Planetary Sciences, California Institute of Technology, Pasadena, California, USA.
[3] Now at Department of Geological Sciences, University of California, Santa Barbara, California, USA.
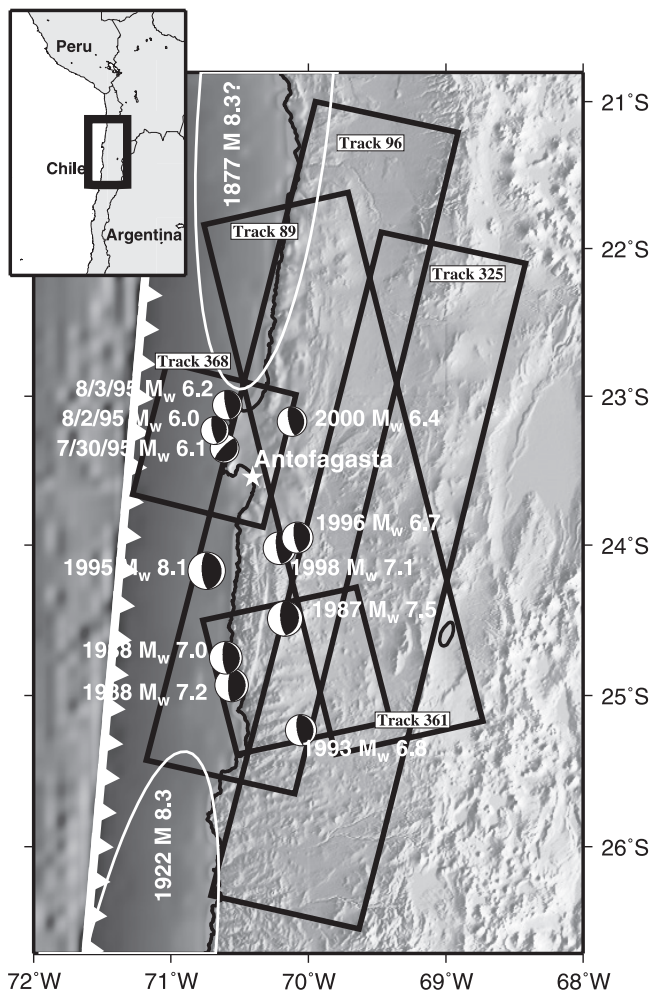
Figure 1. Locations of earthquakes with $M_w > 6$ that probably occurred on the fault interface between 1987 and 2000 in the northern Chile study area. The trench is shown as the barbed white line, and the star is the city of Antofagasta. Mechanisms are from the Harvard CMT catalog, but locations are from the NEIC catalog, except for the 1995 M_w 8.1 event which is from a local network [*Monfret et al.*, 1995]. Earthquake locations from ISC and *Engdahl et al.* [1998] catalogs are within 5 km or so of the NEIC locations. Black squares show the outline of radar coverage used in this study. The white ellipses show the approximate rupture areas of the largest earthquakes adjacent to our study area. The size and spatial extent of the 1877 rupture are especially uncertain [e.g., *Comte and Pardo*, 1991; *Beck et al.*, 1998].

are many measurements of surface deformation, they are all on land, such that slip near the trench is poorly resolved [e.g., *Sagiya and Thatcher*, 1999; *Pritchard et al.*, 2002]. Furthermore, geodetic inversions of fault slip can be oversmoothed (particularly for small, deep events), such that they are too smooth to explain the teleseismic data [e.g., *Wald et al.*, 1996]. Alternatively, in some parameterizations, and for some large earthquakes, the geodetic model is rougher than the teleseismic model [*Segall and Davis*, 1997].

[6] Analysis of teleseismic data presents different problems than analysis of geodetic data. For example, for dip-slip earthquakes, waves radiated from one patch are reflected and can partially cancel the waves radiated from

a different patch. These interference effects can cause a trade-off between the inferred depth of the fault slip and the source time function of the slip [e.g., *Christensen and Ruff*, 1985], such that the along-strike resolution is generally better than the downdip resolution when only teleseismic data are used [e.g., *Carlo et al.*, 1999].

[7] We invert teleseismic and geodetic data sets both separately and jointly using the same fault parameterizations and elastic media to allow comparison of the inferred seismic moment from each method. Indirect comparisons are often cited in the literature, and differences between teleseismic and geodetic moments are used to draw conclusions about the amount of aseismic deformation. However, because these models prescribe the fault planes in different ways (changes in dip, as well as changes in the size and depth of the fault plane can affect the inferred moment) [e.g., *Kanamori and Given*, 1982; *Hartzell and Langer*, 1993], apply different types and amounts of damping (for example smoothing or moment minimization), and use different elastic media (see discussion by *Hearn et al.* [2002]) a direct comparison of most teleseismic and geodetic models is not warranted. In other words, differences between teleseismic and geodetic models are often due to different model parameterizations or permissiveness of the data and not to aseismic slip.

2.1. InSAR Data

[8] The InSAR data that we use for this study is shown in Table 1 with a subset of the interferograms in Figures 2 and 3. When possible, we stack multiple interferograms from the same orbital track. Assuming that sources of noise in the interferograms are uncorrelated in independent interferograms, stacking the interferograms reduces the noise. In this region of Chile, we find that the noise is usually correlated with topography (probably related to vertical stratification of the atmosphere[*Fujiwara et al.*, 1998; *Hanssen*, 2001]), so the spatial pattern of the noise is very similar in independent interferograms, although the sign of the signal does reverse. These atmospheric effects are usually only a few centimeters in amplitude [e.g., *Beauducel et al.*, 2000], and so are much less than the deformation from the 1995 and 1998 earthquakes (tens of centimeters) but are comparable in magnitude to the deformation from the 1993 and 1996 earthquakes.

[9] InSAR data were processed using the publicly available Caltech/JPL ROI_PAC software [*Rosen et al.*, 2004] using the 90-m digital elevation model (DEM) from the Shuttle Radar Topography Mission (SRTM) [*Farr and Kobrick*, 2000]. For all interferograms, we use initial estimates of the orbits calculated by *Scharroo et al.* [1998], and empirically reestimate the baselines. For interferograms that span the 1995 and 1998 earthquakes, we estimate a preliminary model of coseismic deformation, and then calculate the orbital baseline parameters including quadratic baseline terms, as by *Pritchard et al.* [2002], that minimize the phase difference between the interferogram (with the model removed) and a synthetic interferogram made with a DEM [*Rosen et al.*, 1996]. For the other interferograms, we assume that the deformation signal is small (justified below), and find the best fitting baselines. We subsample the interferograms to reduce the number of points from millions to hundreds or thousands with a sampling density proportional to the curvature of the displacement field [*Simons et al.*, 2002].
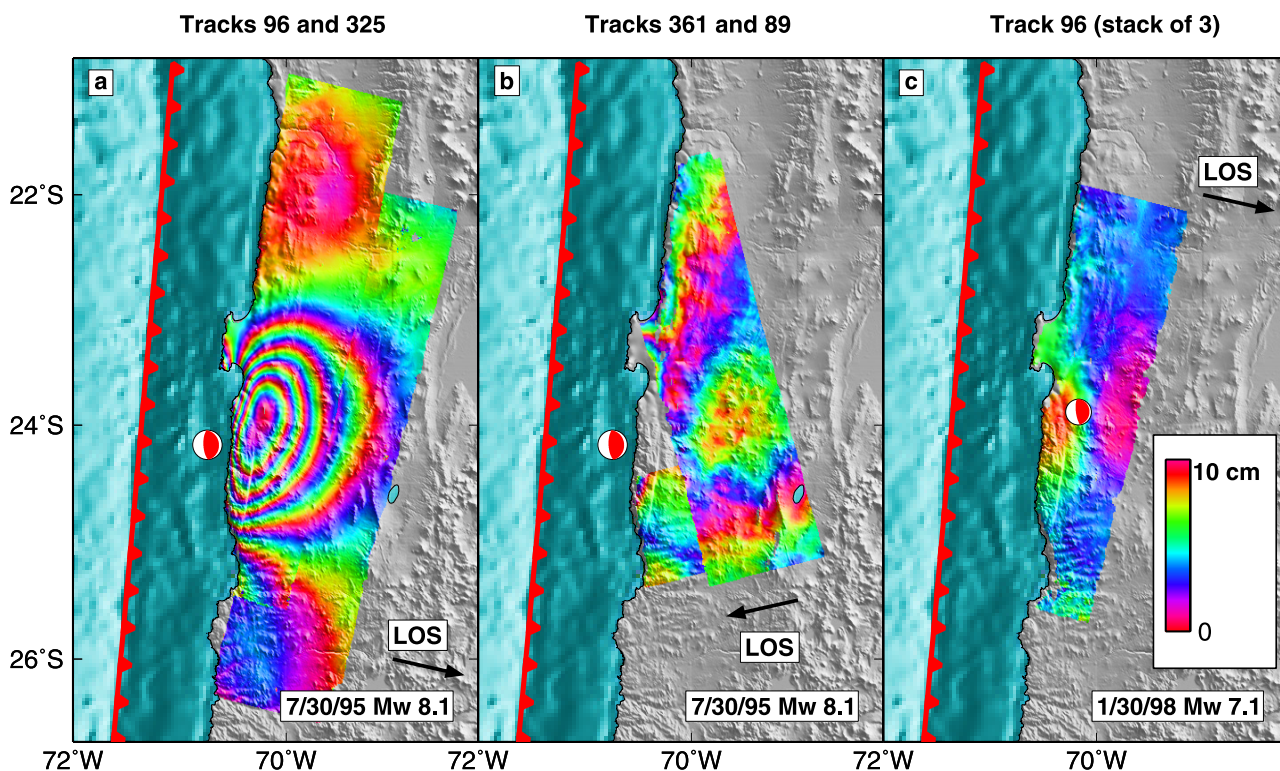
Figure 2. Contours of LOS displacement for the 1995 and 1998 earthquakes. The ground-to-satellite LOS direction is indicated by the arrows. Mechanisms are from the Harvard CMT catalog, but the location of the 1998 earthquake is from NEIC. (a) Two of the three available tracks of descending data for the 1995 M_w 8.1 earthquake. Data from track 96 are from an interferogram spanning 9 October 1995 to 8 May 1992, and data from track 325 are from an interferogram spanning 19 September 1995 to 24 May 1992 (see Table 1 for more information). (b) Two ascending tracks of data for the same earthquake. Interferograms spanning 12 May 1993 to 26 September 1997 and 28 May 1993 to 12 October 1997 were used from tracks 361 and 89, respectively. (c) One of the two tracks of descending data available for the 1998 M_w 7.1. This image is from a stack of three interferograms from track 96 spanning 31 May 1999 to 13 October 1997, 6 March 2000 to 21 April 1997, and 7 December 1998 to 21 April 1997.

[10] For the 1995 earthquake, we use data from five orbital tracks (both ascending and descending) to make 12 interferograms, including an additional track and a few interferograms not used in *Pritchard et al.* [2002]. For the 1998 earthquake, we use a total of five interferograms from two orbital tracks with only descending orbits.

[11] The interferograms spanning the 1993 and 1996 earthquakes have lower signal-to-noise ratios than those for the 1995 and 1998 earthquakes (Figure 3). The 1993 and 1996 earthquakes are about M_w 6.7 and at 50 km depth, so the peak-to-peak line-of-sight (LOS) surface displacement is only $1.5-2$ cm, of the same order as the atmospheric noise. To determine whether the signal in the interferograms is really caused by the earthquakes, we have inverted teleseismic data for these earthquakes (see modeling strategy) and used the resulting slip distributions to make predicted interferograms (Figure 3). The predicted displacement from the teleseismic-derived slip maps has about the same amplitude and location as in the interferograms. For the 1996 earthquake, the pattern that we associate with the earthquake exists in several interferograms, where the atmospheric contamination is both positively and negatively correlated with topography. Although we have only a single interferogram from the 1993 earthquake (from track 325),

the surface deformation predicted by the teleseismic model is consistent with the observed pattern. Because these tests indicate that the deformation patterns are likely caused by these earthquakes, we use the data to perform InSAR-only and joint inversions of slip.

[12] Obtaining a reliable estimate of the coseismic slip for the 1996 event is important because this earthquake could contaminate estimates of postseismic deformation in the existing InSAR and GPS data. For the 1996 earthquake, we use two tracks of data, including nine interferograms. We stack all of the available data from track 325, but track 96 has more noise (as measured by the root-mean square phase variations of the entire interferogram), probably because track 96 is next to the coast (where moisture is often trapped within valleys as fog). We have selected interferograms to stack that span the shortest amount of time around the 1996 earthquake, have the smallest atmospheric contamination, and atmospheric contamination that is both positively and negatively correlated with topography (Table 1).

2.2. GPS Data

[13] There is GPS data spanning the 1993, 1995, 1996, and 1998 earthquakes, but we only use GPS data spanning the 1995 earthquake. Because the GPS measurements are

PRITCHARD ET AL.: EARTHQUAKES IN NORTHERN CHILE

infrequent, the coseismic signals from the 1993, 1996, and 1998 earthquakes are small relative to other deformation signals. GPS data for the 1995 earthquake from the SAGA array (we use 43 stations [*Klotz et al.*, 1999]; Figure 4 shows locations), have been found to be consistent with InSAR observations within a few centimeters [*Reigber et al.*, 1997; *Pritchard et al.*, 2002]. We also use the newly reprocessed GPS data for the 1995 earthquake from a French-Chilean array (9 stations, [*Ruegg et al.*, 1996; *Chlieh et al.*, 2004]) (Figure 4). Direct comparison of this new data and InSAR data is not possible, because vertical GPS displacements were not calculated in the reprocessing.
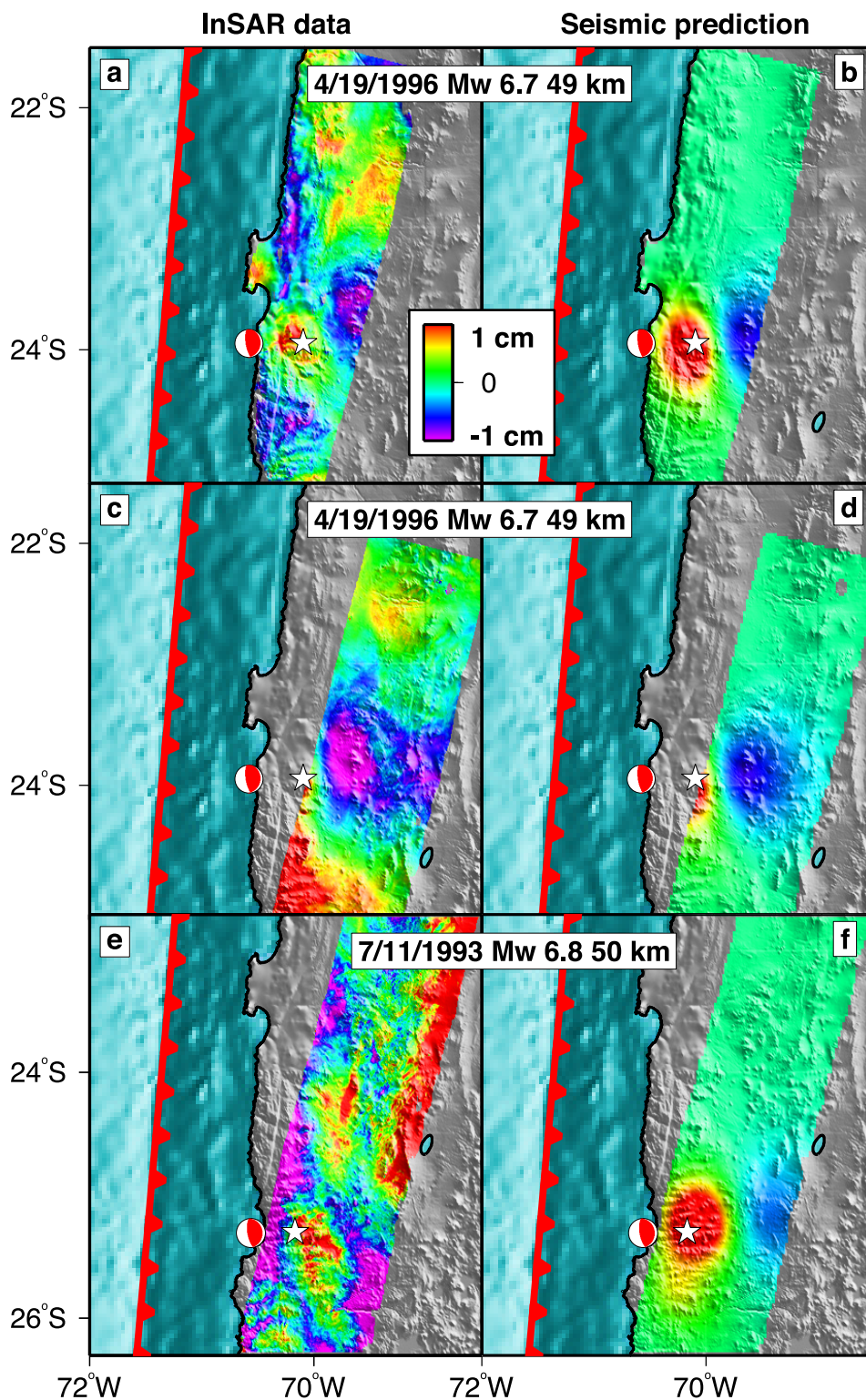

Figure 3

Table 1. ERS Interferograms Used to Constrain Coseismic Deformation From the 1993, 1995, 1996, 1998, and 2000 Earthquakes Near Antofagasta, Chile[a]

Track	Frame(s)	Image 1	Image 2	$B_\perp$, m
		1993 M_w 6.8 Earthquake		
325	4059–4131	24 May 1992	11 Jul 1995	120
96	4041–4113	5 May 1992	9 Oct 1995	50
96	4041–4113	19 Nov 1993	17 Nov 1997	90
96	4041–4131	19 Nov 1993	1 Apr 1996	240
96	4041–4095	16 Apr 1995	8 Oct 1995	110
96	4041–4095	16 Apr 1995	30 Jul 1995	200
		1995 M_w 8.1 Earthquake		
96	4041–4095	16 Apr 1995	13 Oct 1997	20
325	4059–4131	24 May 1992	15 Aug 1995	80
325	4059–4131	24 May 1992	19 Sep 1995	40
325	4059–4131	11 Jul 1995	19 Sep 1995	130
89	6741–6687	28 May 1993	12 Oct 1997	150
361	6687	12 May 1993	26 Sep 1997	25
368	4077	14 Jul 1995	18 Aug 1995	50
		1996 M_w 6.7 Earthquake		
96	4059–4113	31 Mar 1996	21 Apr 1997	90
96	4059–4113	1 Apr 1996	21 Apr 1997	30
96	4059–4113	31 Mar 1996	2 Dec 1996	130
96	4059–4113	31 Mar 1996	17 Nov 1997	250
96	4059–4113	1 Apr 1996	17 Nov 1997	130
325	4059–4131	19 Sep 1995	21 May 1996	10
325	4059–4131	15 Aug 1995	21 May 1996	30
325	4059–4131	19 Sep 1995	22 May 1996	80
325	4059–4131	15 Aug 1995	22 May 1996	110
		1998 M_w 7.1 Earthquake		
96	4059–4113	13 Oct 1997	8 Aug 1999	90
96	4059–4113	21 Apr 1997	6 Mar 2000[b]	110
96	4059–4113	13 Oct 1997	31 May 1999	90
		2000 M_w 6.4 Earthquake		
96	4059–4113	17 Nov 1997	6 Mar 2000	260
96	4059–4113	7 Dec 1998	6 Mar 2000	80

[a]$B_\perp$ is the perpendicular baseline between the two satellite images used to make the interferogram, and a larger $B_\perp$ means that the interferogram is more sensitive to topographic relief [e.g., *Rosen et al.*, 2000].

[b]This pair was also used in the interferometric stack to look for the 2000 earthquake, once we removed the model of the 1998 earthquake.

2.3. Teleseismic Data

[14] For all earthquakes, we analyze the digital P and SH teleseismic displacement records from the global network [*Butler et al.*, 2004] at epicentral distances between 30° and 90°. We select stations with as uniform an azimuth distribution as possible (Figures 5–8), and create displacement records by deconvolving the station response and integrating. All data are then resampled to 0.2 s after low-pass filtering to less than 1 Hz using a two-pass Butterworth filter.

[15] For the 1995 earthquake, we use teleseismic records that are 125 s long, although we cut the record shorter at a few stations to avoid the PP phase and nonrupture features discussed by *Ihmlé and Madariaga* [1996]. They observe that this earthquake excited large amplitude, nearly monochromatic (14 s) oscillations on seismographs at all azimuths following the P wave, possibly caused by reverberations in the water column near the rupture area in the trench. These oscillations do not become obvious in most records until after about 100 s, while the majority of moment release is in the first 70 s. Furthermore, such waves are caused by three-dimensional structure and cannot be adequately recreated in our one-dimensional model. When the oscillations appar-

Figure 3. (a) Five interferogram stack from track 96 for the 1996 earthquake (see Table 1 for dates). For this and other stacks, the interferograms were combined and then georeferenced. The NEIC location is shown as a white star, and the focal mechanism is from the Harvard CMT catalog. (b) Predicted LOS displacement from this earthquake from our teleseismic-only inversion. For all tracks, the 1993 and 1996 teleseismic-only model predictions of the LOS are visually similar to the geodetic-only and joint results. For track 96, the RMS differences between the data and models are geodetic, 0.20 cm; joint, 0.22 cm; teleseismic model 0.22 cm (to make the comparison equivalent to the geodetic and joint results, we did not just difference the data and model, but also calculated the best fit orbital ramp parameters). (c) Four interferogram stack from track 325 (Table 1). (d) Predicted surface LOS displacements from our teleseismic inversion for this track. For track 325, the RMS difference between the models and data are geodetic, 0.18 cm; teleseismic, 0.20 cm; joint, 0.19 cm. (e) The only interferogram we have that spans only the 1993 earthquake (track 325). (f) Predicted LOS displacements from teleseismic slip inversion. The RMS difference between the data and the geodetic model is 0.43 cm, while the RMS for both the teleseismic and joint models is about 0.47 cm.
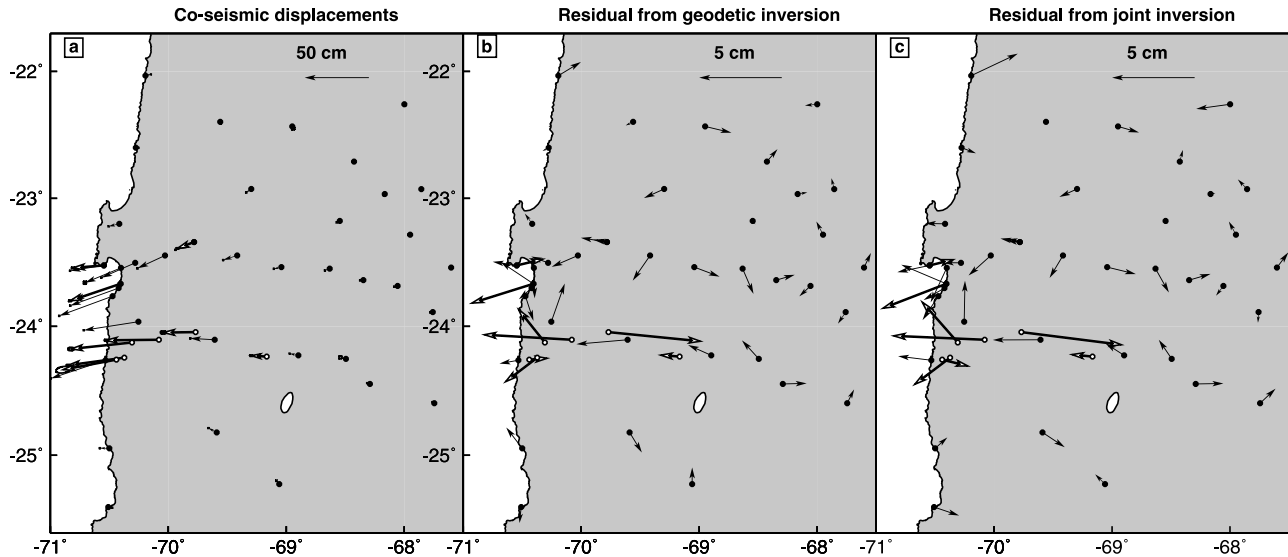
Figure 4. (a) GPS displacements from the SAGA (black circles) and French-Chilean (white circles with black outlines) arrays. (b) Difference between the GPS displacements and the predicted displacements from our geodetic-only model of slip in the 1995 earthquake. (c) Difference between the data and the joint model. RMS values are as follows (geodetic-only, joint, teleseismic-only inversions): SAGA GPS east (1.1 cm, 1.4 cm, 12.2 cm); SAGA GPS north (0.89 cm, 0.87 cm, 5.1 cm); SAGA GPS vertical (1.2 cm, 1.3 cm, 9.9 cm); French-Chilean GPS east (3.2 cm, 3.4 cm, 11.7 cm); French-Chilean GPS north (1.0 cm, 1.2 cm, 3.9 cm).

ently contaminate a record, we cut the record short, as shown in Figure 6. We use 14 P and 12 SH records for the 1995 earthquake (Figure 6). For the 1993, 1996, and 1998 earthquakes we use records 60 s long (Figures 5, 7, and 8). We use only teleseismic data to model the rupture of three $M_w > 6$ aftershocks within a few days of the 1995 main shock, and a M_w 6.4 event in 2000 (Figure 1). The aftershocks are M_w 6.1 on 30 July 1995 at 2105 UT; M_w 6.0 on 30 July 1995 at 0014 UT; and M_w 6.3 on 3 August 1995 at 0157 UT. For the three events, we use between $10-11$ P records and $8-10$ SH records.

3. Modeling Strategy

[16] Several studies have combined seismic data with GPS [e.g., *Wald and Heaton*, 1994; *Ji et al.*, 2002b, 2003] and InSAR [e.g., *Hernandez et al.*, 1999; *Kaverina et al.*, 2002; *Delouis et al.*, 2002; *Salichon et al.*, 2003] to study earthquake rupture. We use the technique of *Ji et al.* [2002a] (hereinafter called the Ji method) to invert for fault slip using both the teleseismic waveforms and geodetic data. Details of the Ji method, including tests of the resolving power are given by *Ji et al.* [2002a], and here we only provide a brief summary. The teleseismic waveforms are transformed into the wavelet domain so that both the temporal content (which contains information about the spatial location of slip) and frequency content (which constrains the duration of rupture on each patch, also called the risetime) of the waveforms are used.

[17] For the location and dip of the fault plane in our inversions, we slightly perturb the fault plane of *Pritchard et al.* [2002] which is well defined by aftershocks of the 1995 earthquake located with onshore and offshore stations [*Husen et al.*, 1999; *Patzig et al.*, 2002]. For the 1993, 1996,

and 1998 earthquakes we use only a subsection of the fault plane, and assume the fault has a uniform dip in each segment. We find that the best fitting model for each earthquake has a slightly different dip. Since the exact geometry for the larger 1995 earthquake is not known and the slip distribution depends on the model parameterization [*Hartzell and Langer*, 1993], we test a variety of fault geometries with up to three segments with different dips. We use a one-dimensional (1-D) layered velocity model with 14 layers [*Husen et al.*, 1999]. We also test models with a much simpler velocity structure (only a crust and mantle), and models with a water layer at the top. We do not simultaneously solve for the fault location and slip parameters (e.g., risetime, rupture velocity, slip direction and magnitude) because it would be computationally prohibitive to solve for all these parameters simultaneously. Further, given the nonuniqueness in the teleseismic inversion for the large earthquakes and the inability of the geodetic data to resolve fine variations in the fault dip, it is not clear that an inversion for fault plane parameters with these data sets would supercede the aftershocks studies.

[18] For each subfault, we solve for the slip amplitude and direction, risetime and rupture velocity. The risetime indicates the length of time it takes for the fault patch to slip (prescribed as a modified cosine function [*Hartzell et al.*, 1996]) and the rupture velocity specifies the speed of the local rupture front. For each parameter, we specify extremal bounds and a discretization interval. We discretize the fault with uniform patches, but tested several different subfault sizes and configurations.

[19] We solve for quadratic ramps in the InSAR and GPS data to correct for orbital errors not removed through baseline reestimation (see InSAR data section) and interseismic deformation in both geodetic data sets. Because
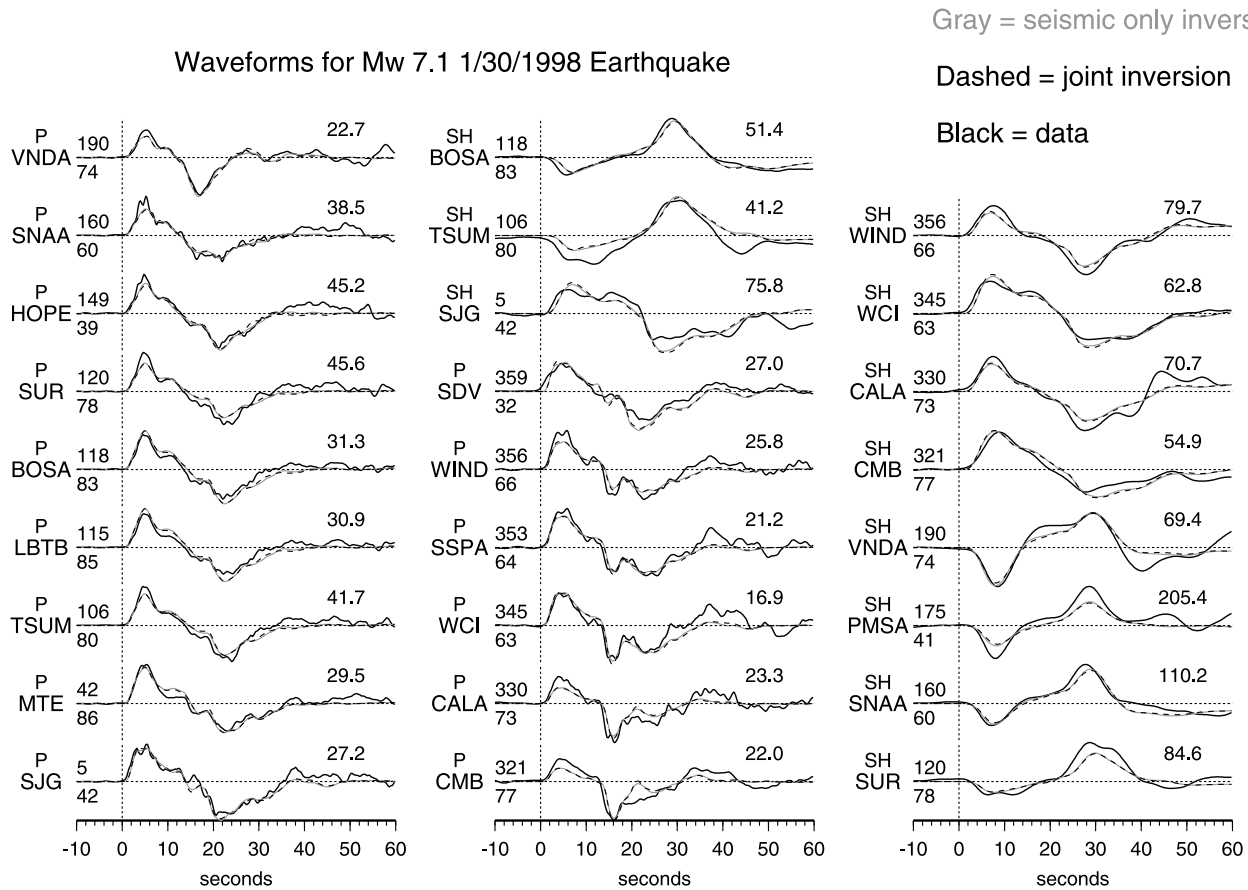
Figure 5. P and SH displacements as a function of time in seconds used in the slip inversion for the 1998 M_w 7.1 earthquake (black lines) and calculated synthetics from the teleseismic-only (gray lines) and joint inversions (black dashed lines). To the left of each trace is the station name, epicentral distance (lower number) and azimuth (upper number), both in degrees. The type of record (P or SH) is listed above each station name. Each amplitude has been normalized by the maximum displacement for that record, shown in microns to the upper right of each trace.

some of the GPS and InSAR data that span the 1995 earthquake also include deformation from the 1993 and 1996 earthquakes, we remove our joint models of these smaller events before inverting for slip from the 1995 earthquake.

[20] We define the best fit model as having the lowest objective function, given as $E_{wf} + W_I * E_I + W_S * S + W_M * M$, where E_{wf} is the waveform misfit (calculated for each wavelet channel with different weighting), E_I is the geodetic misfit, S is a normalized, second derivative of slip between adjacent patches (smoothing), M is a normalized seismic moment, and W_I, W_S, and W_M are the relative weighting applied to the geodetic misfit, smoothing, and moment, respectively. The least squares misfits are calculated for the teleseismic and geodetic data. For the teleseismic misfit, the SH waves are weighted twice as much as the P waves, because we found that such additional weighting was necessary in our inversion scheme to achieve a better fit to the fewer SH records used. In addition, the SH waves generally contain fewer oscillations than the P waves (in part because the P waves have less attenuation), such that to minimize misfit the inversion typically tries to better fit the P wave records.

[21] There is some ambiguity to picking the appropriate weighting between data sets [e.g., *Kaverina et al.*, 2002]. We tested different values of W_I, but found that using equal

weighting between the waveform and geodetic misfits did not significantly degrade the fits to the teleseismic or geodetic data between the individual and joint inversions given the normalizations employed by the Ji method. The Ji method normalization explicitly accounts for the different amplitudes of each term in the objective function to allow for fast application of the technique to earthquakes of various sizes and types. For example, the geodetic misfit is premultiplied by a term that accounts for the relative sizes of the E_{wf}, E_I, and W_S terms [*Ji et al.*, 2002b]. For a well-constrained inversion, moment weighting should not be necessary, and so we chose W_M to be zero, although we use a nonzero moment weighting for the teleseismic and joint inversions for the 1995 earthquake as we discuss in a later section (Table 2). The value for W_S is the same as in other applications of the Ji method (Table 2) [*Ji et al.*, 2002b, 2003], and values within an order of magnitude have little impact on the waveform fit or the broad features of the slip distributions although smaller values make the distribution unrealistically rough. Other inversion details are available in *Pritchard* [2003].

[22] We use a simulated annealing algorithm [e.g., *Rothman*, 1986] to find the best fitting model parameters for the teleseismic, geodetic and joint inversions for coseismic slip. This nonlinear, iterative inversion algorithm is
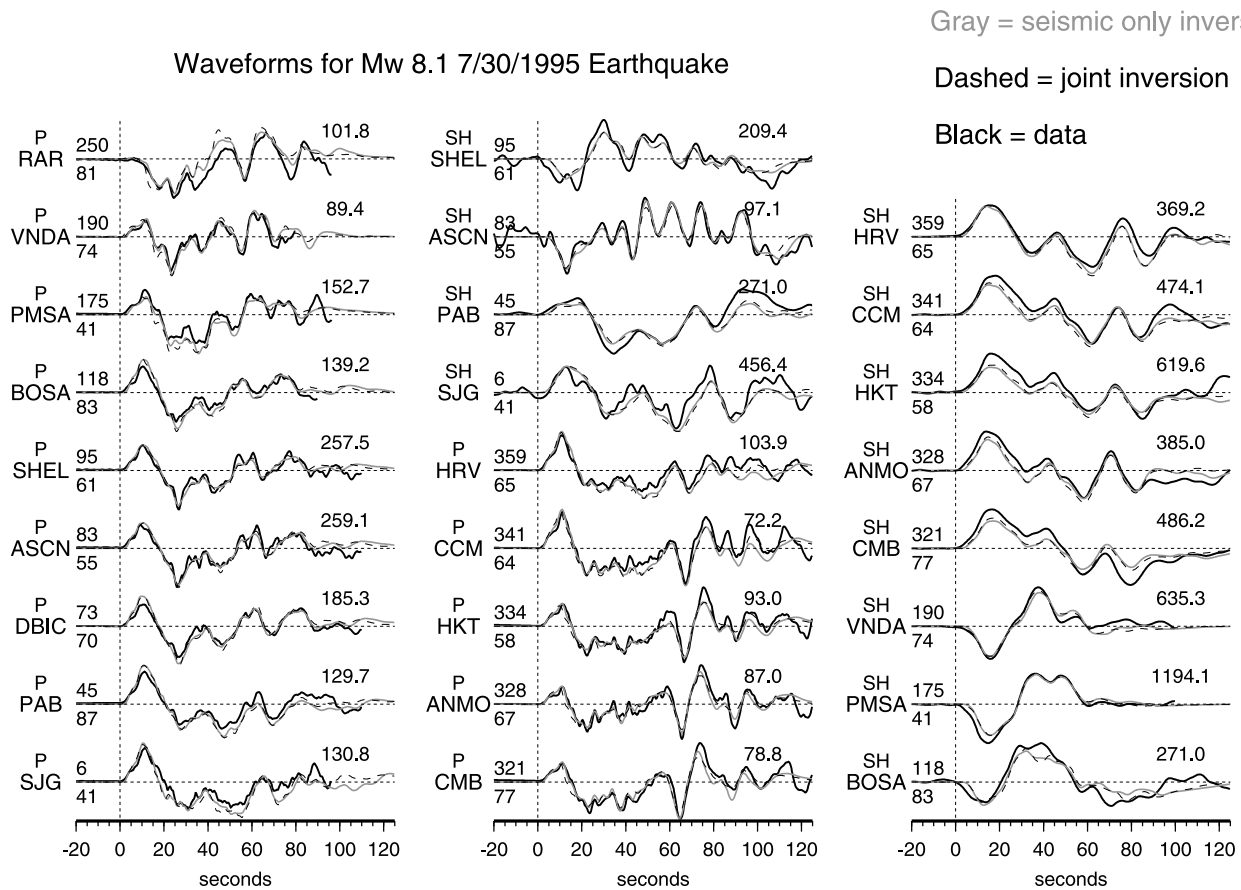
Figure 6. Teleseismic data (P and SH displacements as a function of time in seconds) used in the slip inversion for the 1995 M_w 8.1 earthquake (black lines) and calculated synthetics from the teleseismic-only (gray lines) and joint inversions (black dashed lines). Conventions are the same as in Figure 5.
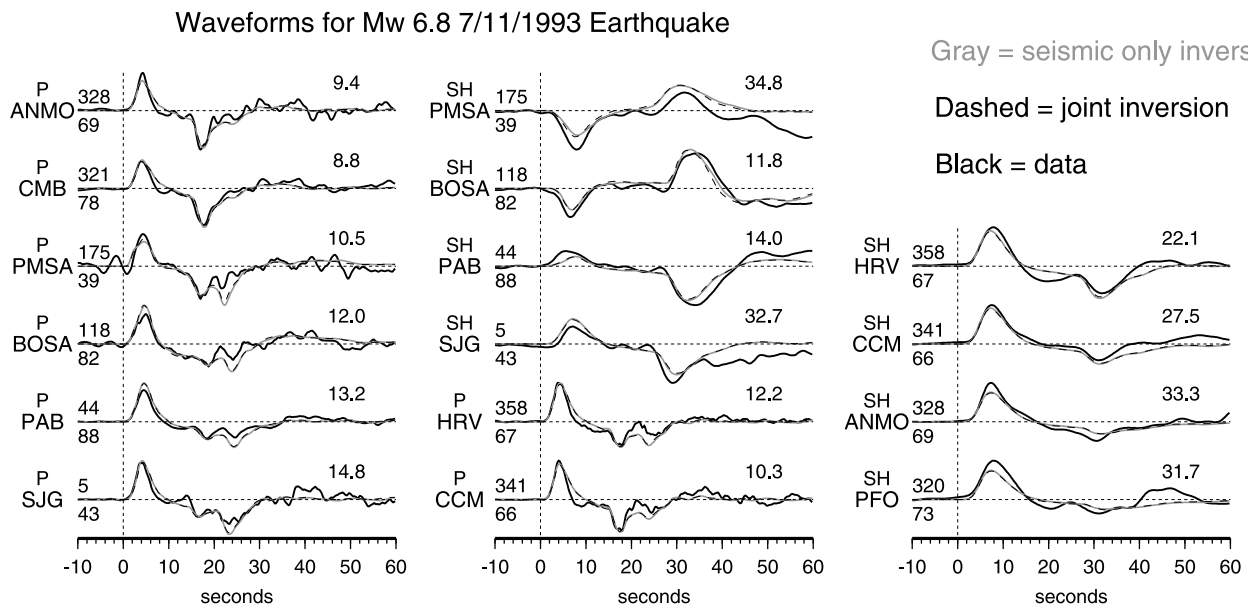
Figure 7. Teleseismic data (P and SH displacements as a function of time in seconds) used in the slip inversion for the 1993 M_w 6.8 earthquake (black lines) and calculated synthetics from the teleseismic-only (gray lines) and joint inversions (black dashed lines). The teleseismic-only and joint seismograms are almost identical. Conventions are the same as in Figure 5.
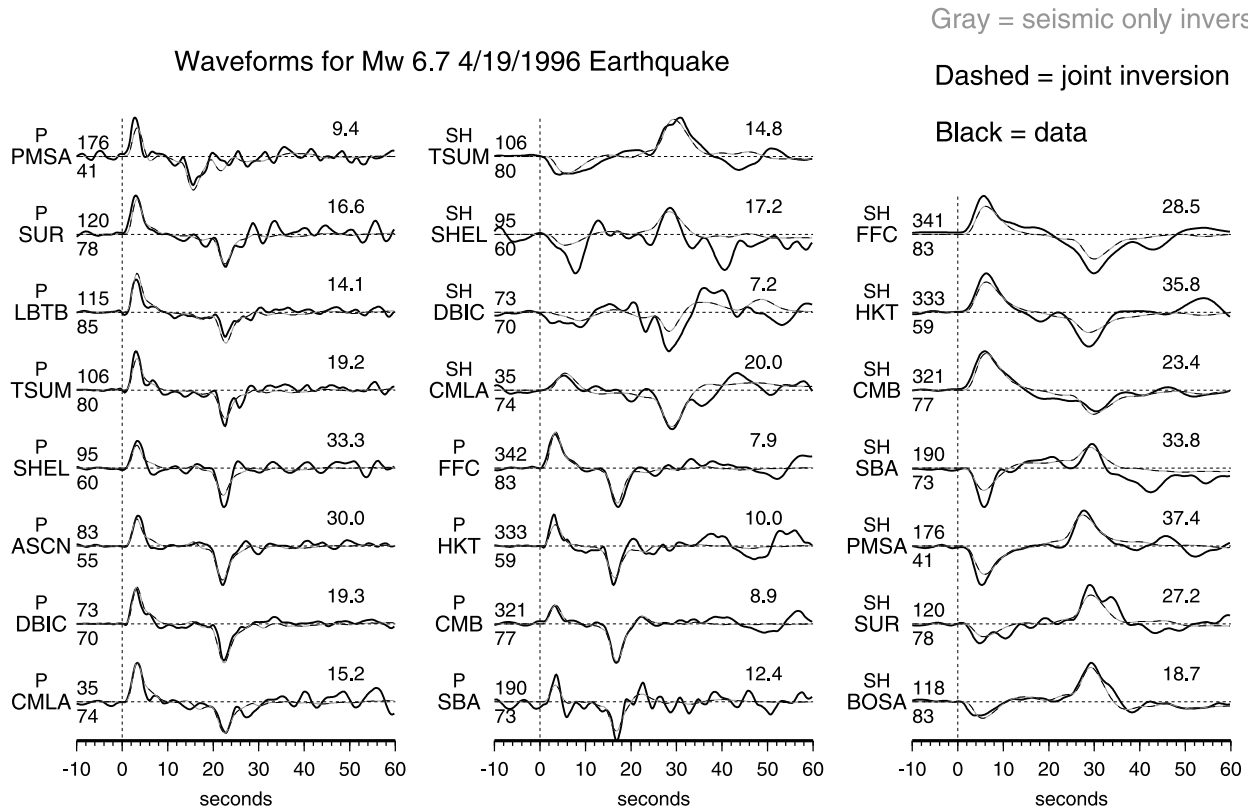
Figure 8. Teleseismic data (P and SH displacements as a function of time in seconds) used in the slip inversion for the 1996 M_w 6.7 earthquake (black lines) and calculated synthetics from the teleseismic-only (gray lines) and joint inversions (black dashed lines). The teleseismic-only and joint seismograms are almost identical. Conventions are the same as in Figure 5.

designed to avoid local minima by searching broadly through parameter space in initial steps, and then in later iterations to focus on regions that well fit the data [e.g., *Sen and Stoffa*, 1995]. This algorithm requires deciding how to transition from the global to detailed search of parameter space, a.k.a. the cooling schedule [e.g., *Basu and Frazer*, 1990]. However, because the objective function has been normalized in the Ji

method, the values chosen by *Ji et al.* [2002b] appear robust for the earthquakes studied here.

4. Results
4.1. The 1998 Earthquake
[23] Contours of slip on the fault interface from the teleseismic-only, geodetic-only, and joint inversions are

Table 2. Model Inversion Results

Event	Moment, N m [M_w] Seismic	Geodetic	Joint	R[a]	T[b]	V[c]	W_S[d]	W_M[e]	X[g]	Y[h]	Δ[i]	D[j]
1993	2.0×10^{19} [6.8]	2.7×10^{19} [6.9]	1.8×10^{19} [6.8]	104°	3	3.2	0.1	0	13	16	5	30°
1995	1.8×10^{21} [8.1]	1.8×10^{21} [8.1]	1.8×10^{21} [8.1]	105°	9	3.1	f	f	16	26	10	N/A[k]
30 Jul 1995	1.5×10^{18} [6.1]	N/A	N/A	101°	2.2	3.2	0.1	0	15	20	2	15°
2 Aug 1995	1.1×10^{18} [6.0]	N/A	N/A	102°	2.4	3.1	0.1	0	15	20	2	20°
3 Aug 1995	3.0×10^{18} [6.2]	N/A	N/A	103°	2.6	3.1	0.1	0	15	20	2.5	17°
1996	1.5×10^{19} [6.7]	1.6×10^{19} [6.7]	1.4×10^{19} [6.7]	107°	3.5	3.1	0.1	0	10	20	5	23°
1998	6.1×10^{19} [7.1]	6.5×10^{19} [7.1]	6.1×10^{19} [7.1]	102°	3.5	3.1	0.1	0	10	20	5	23°
2000	4.5×10^{18} [6.4]	N/A	N/A	103°	3.2	3.1	0.1	0	10	20	2.5	20°

[a]Mean rake.
[b]Mean risetime (seconds).
[c]Mean rupture velocity (km/s).
[d]Weight of smoothing constraint.
[e]Weight of moment minimization constraint. All mean values are for the joint inversion and calculated using weighted averages (weighted by the slip).
[f]The smoothing and moment minimization weights were variable for these inversions (see text).
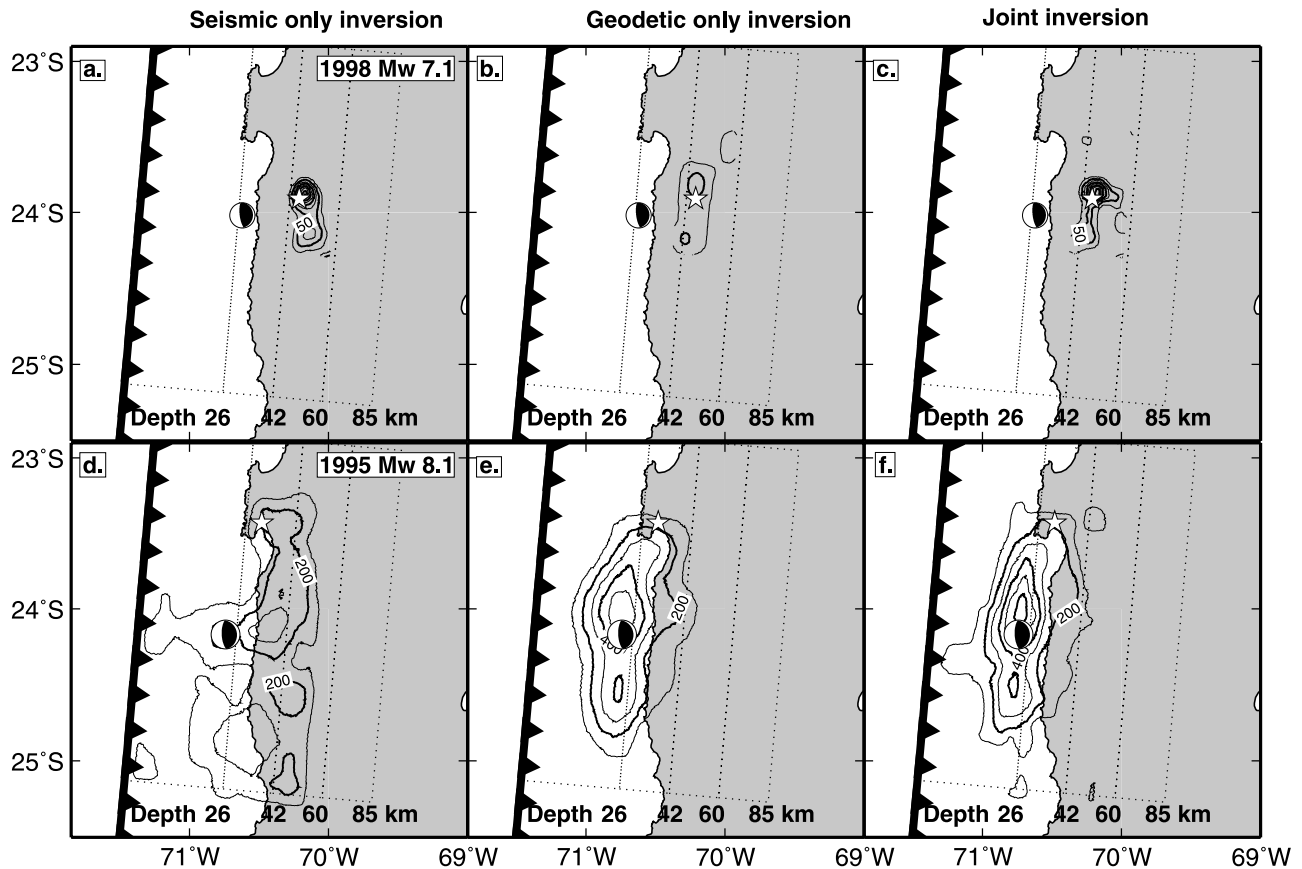[g]Number of subfaults downdip.
[h]Number of subfaults along strike.
[i]Subfault size, same in both dimensions (km).
[j]Dip of fault plane. For the 1995 earthquake, the fault has a change in dip with depth (see text).
[k]N/A, not applicable.

Figure 9. Contours of slip from the 1998 M_w 7.1 earthquake from inversions using (a) only teleseismic data, (b) only InSAR data, and (c) both data sets. The maximum slip is about 2 m, and the contour interval is 0.25 m. Even though the maximum slip (and hence contour density) is higher in the seismic-only model than in the geodetic-only model for the 1998 earthquake, the moment from the geodetic-only inversion is higher because of the greater area that slipped (Table 2). Contours of slip from the 1995 M_w 8.1 earthquake from inversions using (d) only teleseismic data, (e) only InSAR/GPS data, and (f) both data sets. The maximum slip is about 6.5 m, and the contour interval is 1 m. The focal mechanisms are from the Harvard catalog, and the white star shows the hypocenter which is determined to be the NEIC location for the 1998 earthquake and determined from a local network for the 1995 earthquake [Monfret et al., 1995].

shown in Figure 9, and average rupture parameters (moment, rupture velocity, risetime, and rake) from the inversions are in Table 2. For all three inversions, most of the slip is near the hypocenter (as determined by the NEIC), but slip is more concentrated in the teleseismic and joint models (which both have smaller seismic moments than the geodetic-only inversion). The maximum slip was constrained to be less than 3 m, and is about 2.4 m for the teleseismic and joint inversions and about 0.5 m for the geodetic inversion. These inversions were damped only with smoothing, not moment minimization (Table 2). The lower moment slip distribution from the joint inversion fits the InSAR data nearly as well as the geodetic-only inversion (Figure 10), and there is no significant degradation in fit to the teleseismic data in going from the teleseismic-only to joint inversions (Figure 5).

[24] While the mean value of the rake (102°, constrained to be between 70° and 140° in the inversion) is similar to the Harvard CMT value of 105° [Dziewonski et al., 1999], the Harvard CMT location is about 40 km west of the centroid of our model. This systematic westward shift of the

CMT location is also seen for the 1993 and 1996 earthquakes. In this area, the angle of plate convergence is also about 102° [Angermann et al., 1999]. For the 1998 earthquake, the results shown are for a dip of 23° and strike of 5°, but we found that the results changed little for reasonable variations of this parameter (e.g., Harvard dip of 17°, and strike of 8°).

[25] Inclusion of orbital ramp parameters in the inversion has significant impact upon our results, because the long-wavelength deformation signal from deeper events is similar to potential long-wavelength errors in the orbital parameters [e.g., Zebker et al., 1994]. When ramp parameters were not included in the inversion, the geodetic-only slip maps included spurious features to explain the long-wavelength orbital errors, and as a result, the moment for the geodetic-only and joint inversions was much higher than the results shown here [Pritchard, 2003].

4.2. The 1995 Earthquake

[26] The spatial distributions of slip from our inversions are shown in Figures 9 and 11, and the average rupture parameters are in Table 2. There are differences between the
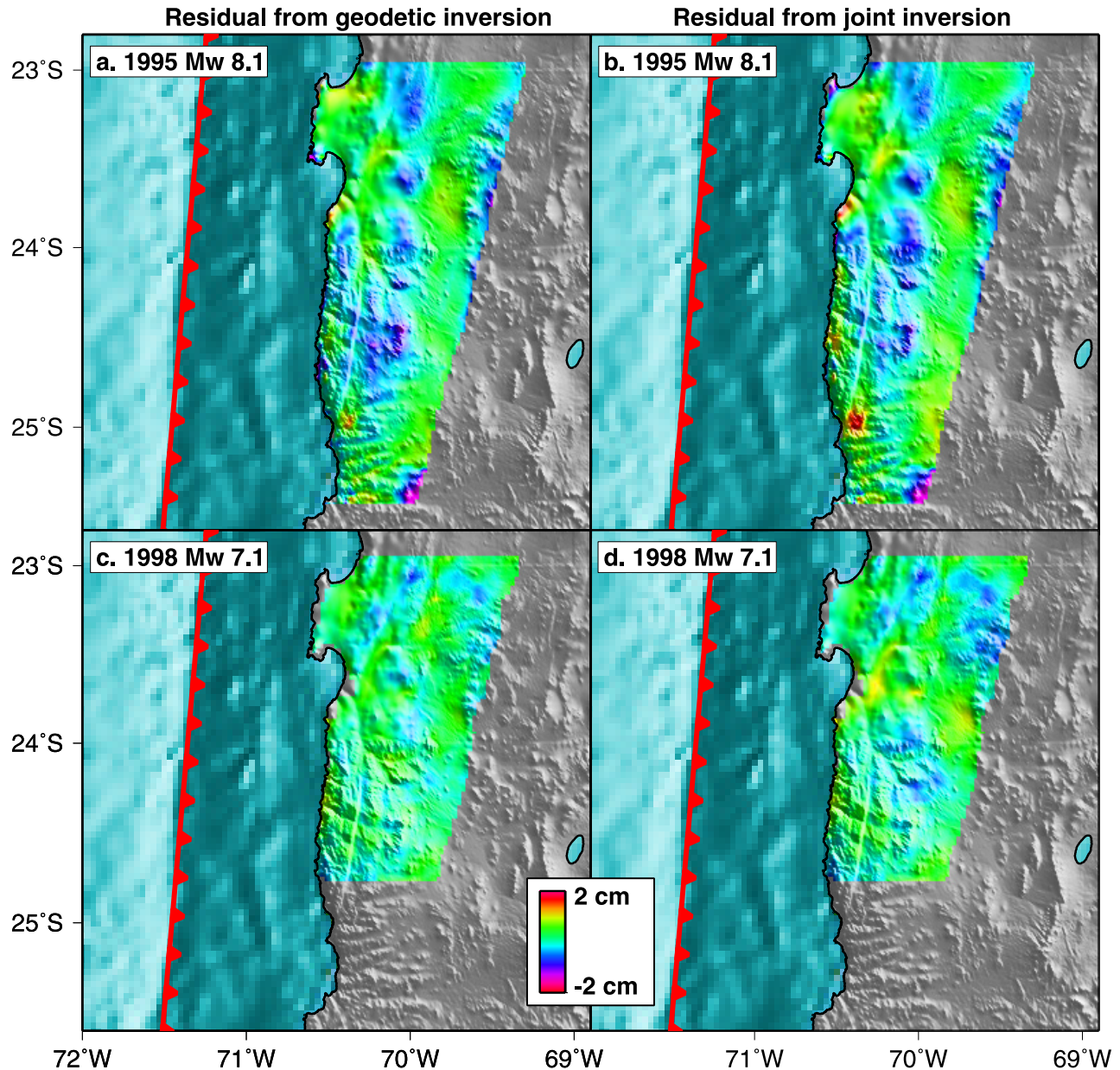
Figure 10. (a and b) InSAR residual from track 96 for the 1995 earthquake using only the geodetic data (Figure 10c, RMS 0.63 cm) and both teleseismic and geodetic data (Figure 10d, RMS 0.66 cm). The residuals from the other tracks are as follows (RMS, geodetic-only, joint, teleseismic-only inversions): track 368 (0.76 cm, 0.81 cm, 5.7 cm); track 325 (0.39 cm, 0.50 cm, 4.0 cm); track 89 (0.83 cm, 0.90 cm, 4.2 cm); track 361 (0.72 cm, 0.95 cm, 3.6 cm); and track 96 (11.5 cm for the teleseismic-only model). (c and d) InSAR residual from track 96 for the 1998 earthquake from the inversions using only the InSAR data (Figure 10a, RMS 0.43 cm) and both teleseismic and InSAR data (Figure 10b, RMS 0.44 cm). The RMS for track 368 is 0.28 cm for both the InSAR-only and joint inversions. For the teleseismic-only inversion, the RMS is 0.31 cm for track 368 and 0.67 cm for track 96.

teleseismic-only and geodetic-only inversions, with the teleseismic model placing more slip at depth (extending to the bottom of the parameterized fault plane), while slip ends abruptly at about 40 km in the geodetic-only and joint inversions. We think that the deep slip in the teleseismic-only inversion is an artifact of the nonuniqueness in the body wave data (e.g., the waveforms from the joint inversion are similar to the teleseismic-only inversion, Figure 6). Previous workers have found that when only teleseismic data are used, the area near the hypocenter is the best

resolved, while areas far from the hypocenter (for example, at the bottom of our parameterized fault) are poorly resolved [e.g., *Ji et al.*, 2002a; *Salichon et al.*, 2003]. The fit to the waveforms is similar if the moment is changed by 20%, so for the inversions for this earthquake only, we have used both smoothing and moment damping. For the teleseismic-only and joint inversions, we include a term in our objective function that minimizes the difference between the moment and the moment from the geodetic-only inversion. The fit to
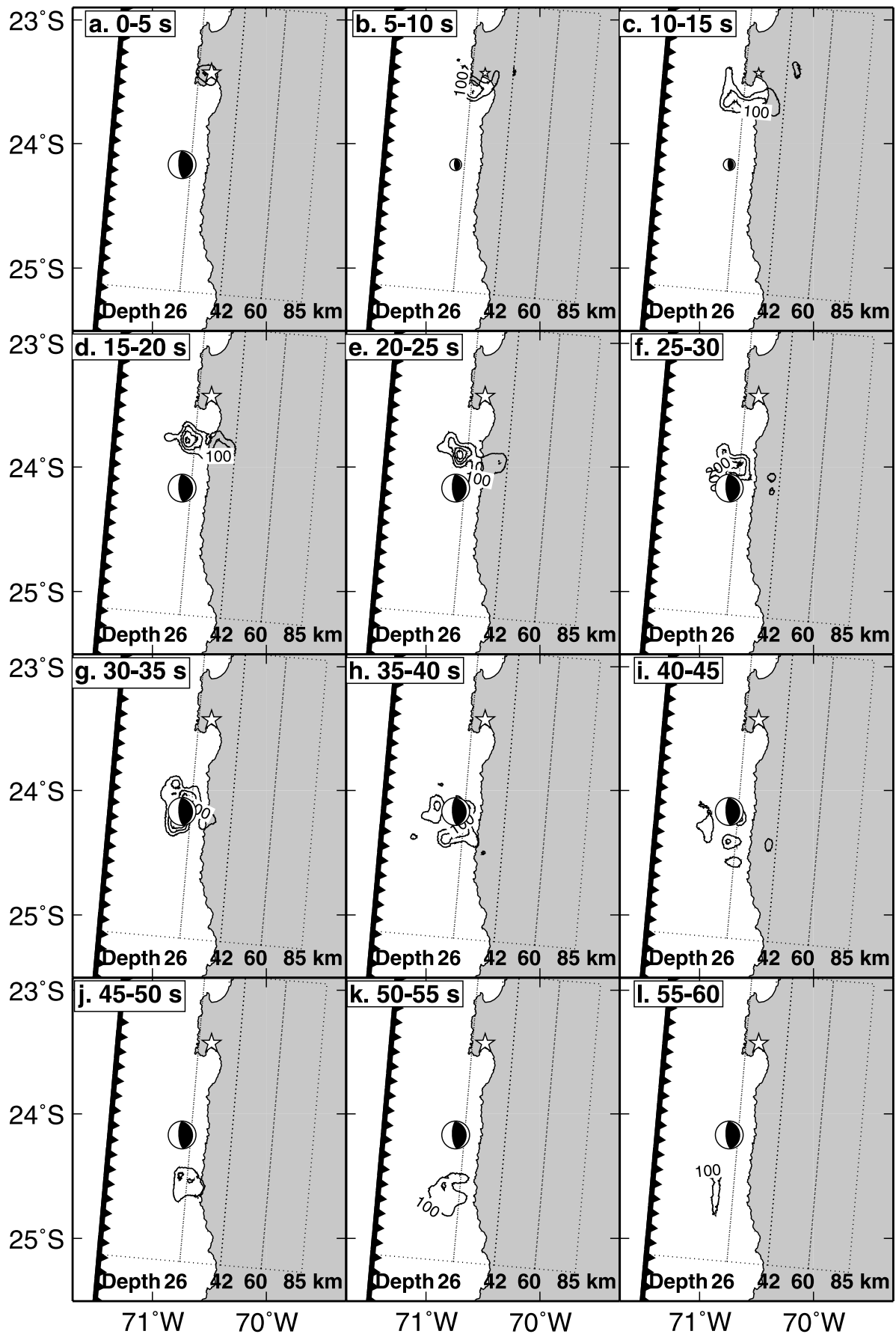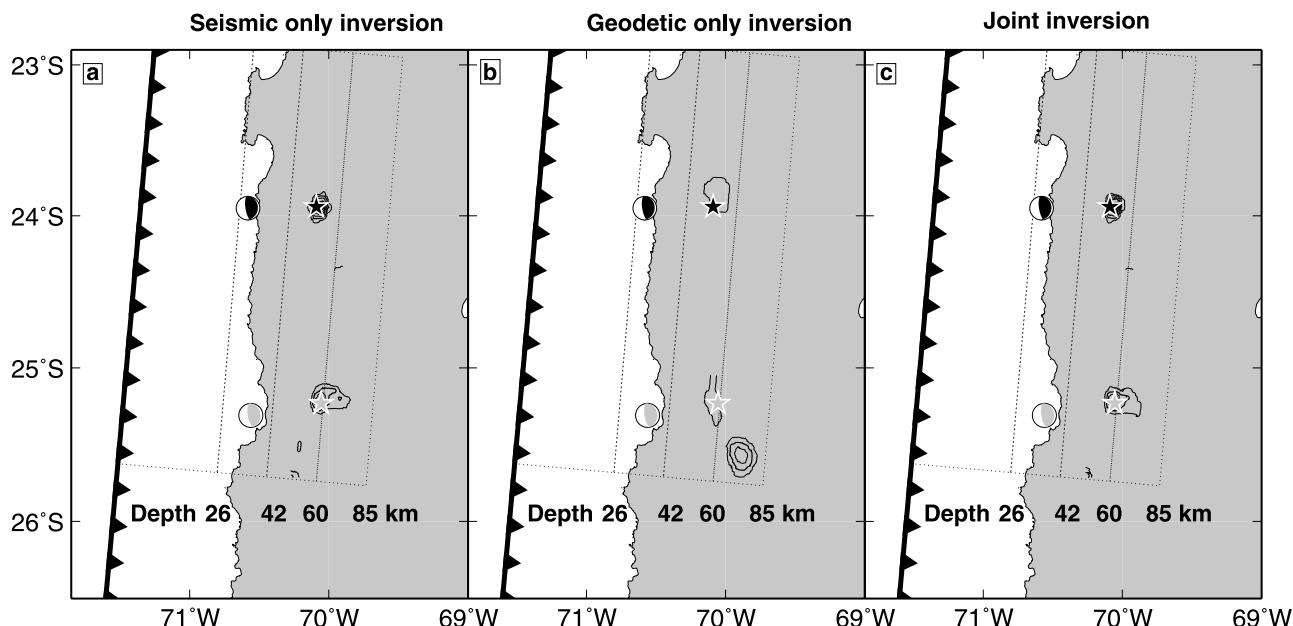
Figure 11

Figure 12. Contours of slip from the 1993 M_w 6.8 and 1996 M_w 6.6 earthquakes from inversions using (a) only teleseismic data, (b) only InSAR data, and (c) both data sets. For both events, the maximum slip is about 1 m, and the contour interval is 0.2 m. The NEIC location is shown as the star, light gray for 1993 and black for 1996. The Harvard CMT for both earthquakes (same colors as for the hypocenters) are located about 40 km from the actual centroid.

the geodetic data is about the same for the geodetic-only and joint inversions (Figures 4 and 10).

[27] Our joint inversion is broadly consistent with previous work [*Ruegg et al.*, 1996; *Ortlieb et al.*, 1996; *Delouis et al.*, 1997; *Ihmlé and Ruegg*, 1997; *Carlo et al.*, 1999; *Klotz et al.*, 1999; *Pritchard et al.*, 2002] in terms of total moment (1.8×10^{21} N m compared with $0.9-2 \times 10^{21}$ N m for previous studies), rake ($105°$ compared to $97-116°$), and rupture velocity (3.1 km/s compared with 2.5–3.2 km/s). Broad features of the distribution of slip are also similar in all models: the rupture is smooth, unilateral to the south (Figure 11), with most moment release near the CMT location, a secondary increase south of the CMT, and little near the hypocenter. Some details of the slip distribution are different from the previous joint teleseismic and geodetic study [*Ihmlé and Ruegg*, 1997]. In particular, slip in our joint model extends more toward the shore and further south. We attribute most of these differences to the more complete spatial coverage of the geodetic data used in our model; for example, the model of *Ihmlé and Ruegg* [1997] did not have geodetic data in the southernmost part of the rupture area and thus surface deformation from this model had a large misfit with the observed interferograms in this area [*Pritchard et al.*, 2002]. Slip near the trench is poorly resolved and other types of data are needed to confidently resolve slip near the trench such as tsunami waveforms or water column reverberations, [e.g., *Satake*, 1993; *Ihmlé and Madariaga*, 1996].

[28] To test the sensitivity of our slip distribution to the model parameterization, we have tried several different configurations of the fault planes and velocity models. We have done these tests for all of our earthquake models, but only discuss the results in detail for the 1995 earthquake, because the large size of this event tends to enhance the effects of model parameterization upon the slip distributions. Figure 9 shows results for a fault plane where the dip increases twice with depth (from $15°$ to $23°$ at 23 km depth; and to $25°$ at 45 km). We have also tested models with only a single dip ($23°$), and a single change in dip (from $15°-23°$), where we have varied the depth where this change occurs. Assuming the final geometry used in Figure 9, we have tested two other velocity models: we have added a water layer to the nominal 1-D layered model [*Husen et al.*, 1999], and have also tested a model with only two velocity layers (crust to 40 km depth, and a mantle below). The broad features of slip are robust to these changes (max depth of slip $\sim$40 km, slip mostly near the Harvard CMT location, etc.), but the details of the slip distribution change. The most important parameter appears to be the depth where the change in dip is imposed. Forcing the dip to change $5-10°$ degrees at a given depth can cause slip to be abruptly curtailed (even though we minimize roughness across this boundary, just as between any other subfaults). This effect is visible in Figure 9f, where slip near the Mejillones Peninsula ends at a depth of about 23 km. However, the termination of slip in the same area at a depth of about 20 km is a robust feature that is also seen inversions where there is no change in dip. In general, the fit to the teleseismic and geodetic data is similar for all models (e.g., the water layer in the 1-D

Figure 11. Spatiotemporal evolution of fault slip during the 1995 earthquake during five second windows with 1 m contours. The hypocenter from the local network is shown as a white star and the mechanism is from the Harvard CMT catalog. Fault slip after 60 s is small.
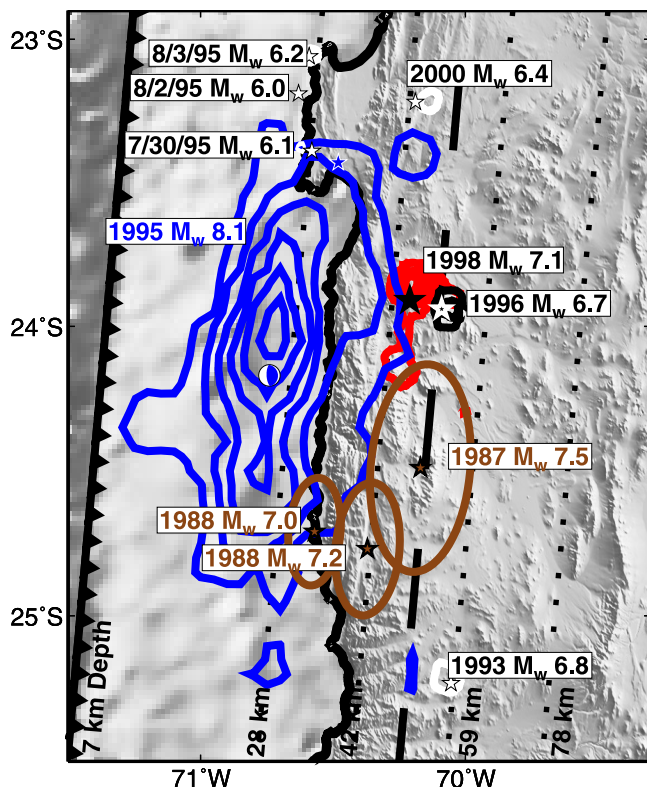
Figure 13. Location of slip on the fault interface in the northern Chile subduction zone from earthquakes with $M_w >$ 6.0 since 1987 plotted over shaded bathymetry and topography. The colored contours are associated with the joint inversions (except for the 1995 aftershocks), and the contour intervals are in parentheses: blue contours are the 1995 earthquake (1 m); white contours are the three large 1995 aftershocks, the 2000 earthquake and the 1993 earthquake (0.5 m); red contours are the 1998 earthquake (0.5 m); and black contours are the 1996 earthquake (0.5 m). The earthquakes from the 1980s are approximated by areas of constant slip (see text) in brown. Depths on the fault interface are exact for the 1995 earthquake (shown as dotted lines and labeled at the bottom), but because some of the other events have slightly different dips, they might be a few kilometers off of the reference depths. The trench is shown as a black barbed line, the coastline is shown as a thick black line, and the depth to full interseismic locking (50 km) is the dashed black line [*Bevis et al.*, 2001].

velocity model has little impact). The fit to the waveforms using the velocity model of [*Husen et al.*, 1999] is perceptibly superior to the two-layer velocity model, but is probably not statistically significant. In summary, our tests of model parameterization indicate that details of the slip distribution can be effected, but broad characteristics (like the depth of rupture) are insensitive to these variations.

4.3. The 1993 Earthquake

[29] Figure 12 shows our inferred slip maps for the 1993 earthquake, and Table 2 contains the average rupture properties. While slip in the teleseismic-only inversion lies close to the hypocenter, large concentrations of slip in the InSAR-only model lie several tens of kilometers away from

it. The signal-to-noise ratio of the InSAR data is very low for this relatively small and deep earthquake (Figure 3), such that there is a large trade-off in solving for slip on the fault plane and the ramp parameters used to account for errors in the satellite orbits. Thus the InSAR data can be explained by a large set of models, including the joint model that has most of the slip at the hypocenter (the teleseismic data are also well fit by both models, see Figure 7).

[30] We test different dips of the fault plane (assuming the depth and strike of the fault are known), and find that the best fitting dip is 30°, constrained by the waveforms. The Harvard CMT dip is 21°, but it does not explain the amplitude of first P pulse at stations between azimuths of about 180°–360°. The larger dip causes a slightly larger misfit to the first SH pulse at BOSA and PMSA, but the improvement to the P fit is much larger and is at more stations. This dip is different from the dips inferred for events at about the same depth, but displaced along-strike (e.g., 1996 and 1998). The along strike variations in dip might indicate local variations of the slab geometry, or that not all of these deep events rupture exactly on the same fault interface.

4.4. The 1996 Earthquake

[31] Results for the 1996 earthquake are shown in Figure 12 and Table 2. As with the 1993 earthquake, for this relatively small and deep event there is a trade-off in fitting the geodetic data with slip on the fault plane and ramp parameters. The trade-off is smaller, because we are able to stack data to reduce noise, and use two different tracks of data (Figure 3), such that the geodetic-only fault slip is more similar to the teleseismic and joint results.

[32] The waveform fits show a trade-off between fitting the P and SH records. We chose a dip of 23° because shallow dips (20°) provided a better fit to the SH than P waveforms (particularly P records around 180° azimuth, and SH records around 330° azimuth), while the opposite was true for steeper dips (e.g., 25°).

4.5. The 1995 Small Aftershocks

[33] Although these quakes contribute little to the total moment release on the subduction interface, we have included them in this study to examine their potential effects on surface deformation. Deformation from these events could influence estimates of postseismic deformation. There is no geodetic data that includes just the deformation from any of the three $M_w > 6$ aftershocks, and so there is uncertainty in their hypocentral location. Horizontal location differences for these events among catalog locations (NEIC, Harvard CMT) and locations from a local network [*Monfret et al.*, 1995] are 10–40 km. We cannot just assume the locations from the local network, because these locations are not available for all events [*Delouis et al.*, 1997]. The teleseismic waveforms do not resolve the hypocentral depth well because of local structure and the signal-to-noise ratio of the waveforms for these small events is low, especially for the event on 30 July 1995. In particular, the water layer thickness varies greatly in this area, and we do not have confidence in our one-dimensional results.

[34] Considering these uncertainties, we adopt the NEIC locations, and estimate depths for the fault interface from the other aftershocks (25 km, but uncertain to 5–10 km; the NEIC depths for all events are 15 km). The largest impact
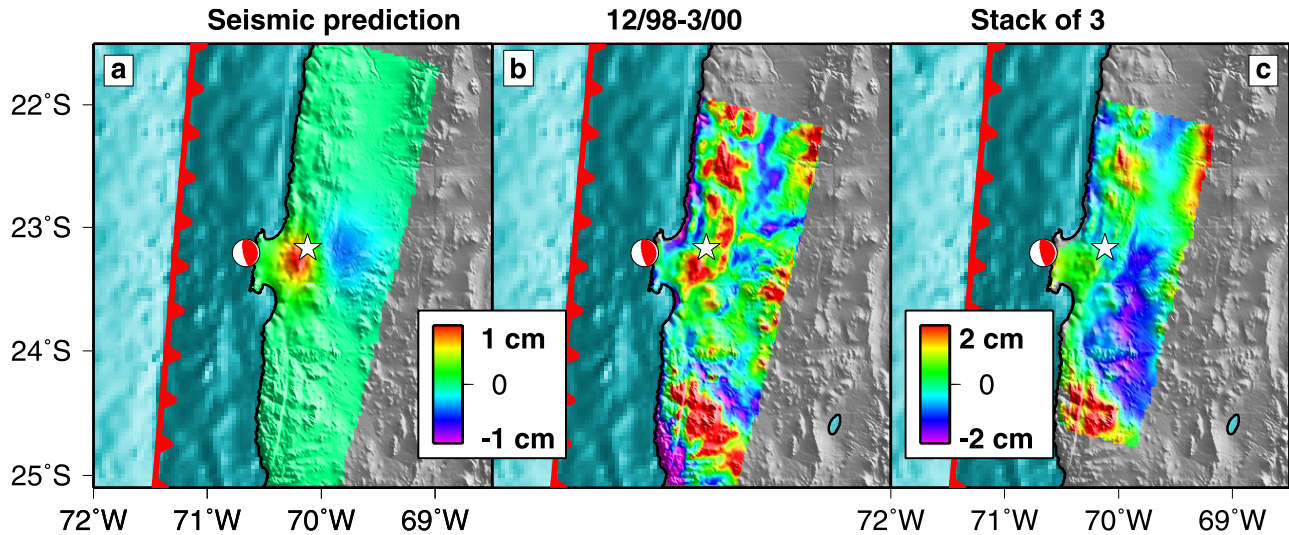
Figure 14. (a) Predicted LOS displacement for the 2000 earthquake from our teleseismic-only inversion. The NEIC location is shown as a white star and the focal mechanism is from the Harvard CMT catalog. (b) Single interferogram that includes only deformation from the 2000 earthquake. (c) Stack of three interferograms from track 96 (see Table 1 for dates). Two of the three interferograms span the 1998 earthquake and have a model of this event removed.

on subaerial surface deformation occurs if the NEIC locations are correct and the earthquakes are located close to shore. Details of the inversions are in Table 2 and slip distributions for the three events are in Figure 13. Because of the small size of these events, we reduced the subfault size to 2.5 km on a side. The maximum subaerial surface deformation assuming the NEIC hypocenters (depth of 15 km) is 3.0 cm (peak-to-peak) in the LOS or 0.1 cm in the horizontal at the nearest GPS station.

4.6. The 2000 Earthquake

[35] Like the 1995 aftershocks, this earthquake contributes little to the seismic moment release, but we include it in our study to test the sensitivity of the geodetic observations, and to ensure that this event does not contaminate inferences of postseismic deformation. The Harvard CMT location is 50 km west of the NEIC and ISC locations, and based on the experience above, we assume the later locations.

[36] Details of the inversions are in Table 2 and the slip distribution is in Figure 13. The maximum subaerial surface deformation when the source depth is 36 km (ISC) is 1.5 cm (peak-to-peak) in the LOS or 0.3 cm in the horizontal at the nearest GPS station. We have three interferograms that span this event, all with the same "after" SAR scene. Only one interferogram has a signal in the right location to be from the earthquake, and the amplitude is similar to atmospheric noise (Figure 14). Therefore we do not detect this earthquake, possibly because the source depth is deeper than 36 km (for example, the NEIC location is at 41 km).

5. Discussion

5.1. Error Analysis

[37] Most attempts at error analysis for slip distributions derived from teleseismic data significantly underestimate the uncertainties for several reasons [e.g., *Beresnev*, 2003]. One problem is that the forward model is always an approximation to reality (i.e., using a 1-D model at the

source and receiver instead of including the realistic 3-D variations [e.g., *Wald and Graves*, 2001]), so that any attempt to completely match the waveforms or the geodetic data is overfitting the data. As we show here for the 1995 earthquake, another issue is that spatiotemporal distributions of slip using only teleseismic data are underdetermined and nonunique for large earthquakes, such that multiple very different models can equally well fit the teleseismic data (Figures 6 and 9) but are not consistent with independent data sets (Figures 10). The approach we use here is to assess which features are robust in inversions of the different data sets and model parameterizations. In addition, for the 1995 earthquake, we can compare our models with those that have used different data sets and modeling assumptions. This is the first study which compares slip distributions from earthquakes of different sizes derived from teleseismic and geodetic data, and thus serves as a useful test case for assessing the accuracy of teleseismically derived slip distributions.

5.2. Teleseismic and Geodetic Inversions

[38] Teleseismic and geodetic data are complementary in constraining fault slip, and this is especially apparent when comparing earthquakes of different sizes. When the signal-to-noise ratio of the geodetic data is low (e.g., for the 1993 and 1996 earthquakes), the slip is not well resolved in geodetic-only inversions, and the teleseismic data serves to localize slip. For large events ($M_w \sim 8$), two-dimensional slip models from the teleseismic-only inversions are not reliable, and the geodetic data helps to reduce the range of acceptable models. In our case, the teleseismic-only inversions fit the geodetic data for the small events, but the fit progressively diminishes for the larger events (see the captions of Figures 3, 4, and 10). For all events, the geodetic-only inversions are smoother than the teleseismic and joint models, because, as other workers have observed, the seismic data requires rougher slip distributions [e.g.,

Wald et al., 1996; *Wald and Graves*, 2001]. In addition, seismic data are more sensitive to slight variations in fault orientation (particularly dip) than geodetic data.

[39] There is a consistent mislocation of the Harvard CMT locations of many of the $6 < M_w < 8$ earthquakes (1993, 1996, 1998, possibly also 1987, 2000, and the 1995 small aftershocks) toward the trench, presumably due to large three-dimensional variations in the velocity structure and the distribution of seismic stations. The fact that the two 1988 earthquakes do not seem to have the same shift as the other events in mysterious. The apparent sensitivity of the CMT location (derived from long-period seismic waves) to 3-D velocity structure does not seem restricted to South America. The NEIC and ISC locations (derived from short-period body waves) appear more accurate (compared to the geodetically inferred locations) for the moderate sized events in northern Chile studied here and in Iran [*Lohman and Simons*, 2004], although these teleseismic locations (especially estimates of depth) can also be in error by tens of kilometers, especially for small and shallow earthquakes [e.g., *Maggi et al.*, 2000; *Pritchard*, 2003; *Lohman and Simons*, 2004]. Previous comparisons of teleseismic locations (e.g., from ISC) to other locations determined in Alaska and the Aleutians has shown a systematic error in the teleseismic locations away from the trench [e.g., *Fujita et al.*, 1981; *Lawton et al.*, 1982], although such systematic variations are not seen in northern Chile [e.g., *Engdahl et al.*, 1998]. In fact, the *Engdahl et al.* [1998] locations for the northern Chile events discussed here are within 5 km or so of the NEIC and ISC locations, although larger shifts between the catalogs are seen in other locations in South America.

[40] We find no systematic variations in the rupture properties as a function of hypocentral depth or event magnitude. Such variations would be hard to believe because the risetime and rupture velocity depend on the velocity model used [e.g., *Ji et al.*, 2002a], and our model is a one-dimensional simplification. Believable spatial variations in the risetime are possible when there is local seismic data, and there is three-dimensional geodetic data on both sides of the fault plane [*Ji et al.*, 2003].

5.3. Comparing Earthquake Slip in Northern Chile

[41] There is only limited overlap between the four recent $M_w > 6.5$ earthquakes in northern Chile (Figure 13). Each earthquake appears to rupture a different part of the fault plane, although the magnitude of slip in each area is different (~5 m in the 1995 event, and <1 m in areas around the 1993, 1996, and 1998 earthquakes). The slip deficit near the small events must be released in other earthquakes or in aseismic slip. Yet, there is little aseismic slip between 1995 and 2000, only 10–20% of the 1995 coseismic moment, and too small to account for the deficit [*Chlieh et al.*, 2004; *Pritchard and Simons*, 2006].

[42] We compare slip between 1993 and 2000 with slip from three $M_w > 7$ earthquakes from the late 1980s. These earthquakes are 5 March 1987, M_w 7.5; 19 January 1988, M_w 7.0; 5 February 1988 (1401 UT), M_w 7.2 (all M_w from Harvard). We have attempted to relocate these events using ISC phase picks, the IASPEI91 traveltimes, and station corrections assuming that the 1998 earthquake location is correct (confirmed by our joint inversions) [*Pritchard*, 2003]. Our relocations agree within error with previous locations [e.g., *Tichelaar and Ruff*, 1991; *Comte and Suárez*, 1995; *Engdahl et al.*, 1998].

[43] To constrain the size of the rupture and the magnitude of slip of the 1980s earthquakes, we use assume a constant stress drop for all of the earthquakes within the study area. Given the seismic moment from our joint inversions and rupture area (we determined both L and W from a plot using 0.1 m contour intervals) for the 1990s earthquakes we calculated the average slip (D) and stress drop ($\Delta \sigma = \mu(D/W)$, assuming that $\mu = 5 \times 10^{10}$ Pa), we found $\Delta\sigma$ between 10 and 20 bars (1 and 2 MPa) for the four events. We also assumed that the ratio between length and width for the 1980s earthquakes was the same as our measured values for the 1990s earthquakes (i.e., $L/W \sim 2$). The seismic moments (all from Harvard) and our calculated average slip are as follows (assuming $\Delta\sigma = 14$ bars): 2.5×10^{20} N m and 1.6 m for 1987; 3.5×10^{19} N m and 0.8 m for January 1988; and 6.6×10^{19} N m and 1 m for February 1988. The earthquakes from the 1980s seem to rupture a different portion of the subduction interface than the 1990s earthquakes and afterslip, as previous workers had observed [*Ihmlé and Ruegg*, 1997; *Delouis et al.*, 1997; *Pritchard et al.*, 2002; *Melbourne et al.*, 2002]. However, again, the slip in the vicinity of the 1980s earthquakes is only a fraction of the maximum slip from the 1995 earthquake, so future earthquakes or aseismic slip are necessary to make up the deficit.

5.4. Downdip Extent of Seismogenic Zone

[44] The 1995 earthquake did not rupture to the bottom of the seismogenic zone (between 40 and 50 km) based on the maximum depth of thrust events on the fault interface [*Tichelaar and Ruff*, 1991; *Suarez and Comte*, 1993; *Tichelaar and Ruff*, 1993; *Comte et al.*, 1994; *Delouis et al.*, 1996; *Husen et al.*, 1999], but the bottom 10 km of depth ruptured in smaller events (1987, 1993, 1996, and 1998). Perhaps variations in material properties as a function of depth, or along strike, do not allow large events to reach the bottom of the seismogenic region, and only small events can occur in that region. Portions of the fault are usually classified as unstable (where earthquakes can nucleate), stable (where earthquakes cannot occur) or conditionally stable (regions where earthquakes can propagate, but not nucleate) [e.g., *Pacheco et al.*, 1993; *Scholz*, 1998]. Obviously the parts of the fault that ruptured during 1996 and 1998 earthquakes are unstable, but perhaps they did not rupture in 1995 because they are surrounded by stable regions. Alternatively, we suspect that the time delay in rupturing these portions of the fault interface (between 1995 and 1996/1998) might be related to time necessary to further load these regions to failure as a result of interseismic deformation, afterslip, fluid flow, and/or postseismic relaxation of the bulk crust and mantle. In particular, a pulse of afterslip between 1997 and 1998 may have triggered the 1998 aftershock [*Pritchard and Simons*, 2006].

[45] The eastern limit of rupture in the 1995 event seems to be roughly similar to the Chilean coastline, as has been observed elsewhere [*Ruff and Tichelaar*, 1996]. The location of the coastline might be related to where the Moho intersects the subducting plate [*Ruff and Tichelaar*, 1996], and so this material interface might effect the downdip seismic limit [*Tichelaar and Ruff*, 1991]. In northern Chile, the downdip limit of seismicity seems to be correlated with

the location of the Moho (40–50 km [e.g., *Patzwahl et al.*, 1999]). In other subduction zones (e.g., Cascadia and Nankai), temperature seems to control the downdip limit (350–450°C), but the northern Chile subduction zone is so cold that these temperatures are not reached until 70 km because of the old age of the Nazca plate, and the lack of insulating sediments [*Oleskevich et al.*, 1999].

References

Angermann, D., J. Klotz, and C. Reigber (1999), Space-geodetic estimation of the Nazca-South America Euler vector, *Earth Planet. Sci. Lett.*, *171*, 329–334.

Basu, A., and L. N. Frazer (1990), Rapid determination of the critical temperature in simulated annealing inversion, *Science*, *249*, 1409–1412.

Beauducel, B., P. Briole, and J.-L. Foger (2000), Volcano-wide fringes in ERS synthetic aperture radar interferograms of Etna (1992–1998): Deformation or tropospheric effect?, *J. Geophys. Res.*, *105*, 16,391–16,402.

Beck, S. L., S. Barrientos, E. Kausel, and M. Reyes (1998), Source characteristics of historic earthquakes along the central Chile subduction zone, *J. South Am. Earth Sci.*, *11*, 115–129.

Beresnev, I. A. (2003), Uncertainties in finite-fault slip inversions: To what extent to believe? (A critical review), *Bull. Seismol. Soc. Am.*, *93*, 2445–2458.

Bevis, M., E. Kendrick, R. Smalley Jr., B. Brooks, R. Allmendinger, and B. Isacks (2001), On the strength of interplate coupling and the rate of back arc convergence in the central Andes: An analysis of the interseismic velocity field, *Geochem. Geophys. Geosyst.*, *2*(11), doi:10.1029/2001GC000198.

Butler, R., et al. (2004), The Global Seismographic Network surpasses its design goal, *Eos Trans. AGU*, *85*(23), 225.

Campos, J., et al. (1995), Estudio del Terremoto de Antofagasta del 30 de Julio de 1995 (in Spanish), *Rep. Prepared Minist. Public Works*, *3733*, 42 pp., Dep. de Geofís., Univ. de Chile, Santiago.

Carlo, D. L., T. Lay, C. J. Ammon, and J. Zhang (1999), Rupture process of the 1995 Antofagasta subduction earthquake ($M_w = 8.1$), *Pure Appl. Geophys.*, *154*, 677–709.

Chlieh, M., J. B. de Chabalier, J. C. Ruegg, R. Armijo, R. Dmowska, J. Campos, and K. Feigl (2004), Crustal deformation and fault slip during the seismic cycle in the north Chile subduction zone, from GPS and InSAR observations, *Geophys. J. Int.*, *158*, 695–711.

Christensen, D. H., and L. J. Ruff (1985), Analysis of the trade-off between hypocentral depth and source time function, *Bull. Seismol. Soc. Am.*, *75*, 1637–1656.

Comte, D., and M. Pardo (1991), Reappraisal of great historical earthquakes in the northern Chile and southern Peru seismic gaps, *Nat. Hazards*, *4*, 23–44.

Comte, D., and G. Suárez (1995), Stress distribution and geometry of the subducting Nazca plate in northern Chile using teleseismically recorded earthquakes, *Geophys. J. Int.*, *122*, 419–440.

Comte, D., M. Pardo, L. Dorbath, C. Dorbath, H. Haessler, L. Rivera, A. Cisternas, and L. Ponce (1994), Determination of seismogenic interplate contact zone and crustal seismicity around Antofagasta, northern Chile, *Geophys. J. Int.*, *116*, 553–561.

Delouis, B., A. Cisternas, L. Dorbath, L. Rivera, and E. Kausel (1996), The Andean subduction zone between 22 and 25° (northern Chile): Precise geometry and state of stress, *Tectonophysics*, *259*, 81–100.

Delouis, B., et al. (1997), The $M_w = 8.0$ Antofagasta (northern Chile) earthquake of 30 July 1995: A precursor to the end of the large 1877 gap, *Bull. Seismol. Soc. Am.*, *87*, 427–445.

Delouis, B., D. Giardini, P. Lundgren, and J. Salichon (2002), Joint inversion of InSAR, GPS, teleseismic, and strong-motion data for the spatial and temporal distribution of earthquake slip: Application to the 1999 İzmit mainshock, *Bull. Seismol. Soc. Am.*, *92*, 278–299.

Dziewonski, A. M., G. Ekström, and M. P. Salganik (1999), Centroid-moment tensor solutions for July–September 1995, *Phys. Earth Planet. Inter.*, *97*, 3–13.

Engdahl, E. R., R. van der Hilst, and R. Buland (1998), Global teleseismic earthquake relocation with improved travel times and procedures for depth determination, *Bull. Seismol. Soc. Am.*, *88*, 722–743.

Farr, T. G., and M. Kobrick (2000), Shuttle Radar Topography Mission produces a wealth of data, *Eos Trans. AGU*, *81*(48), 583, 585.

Fujita, K., E. R. Engdahl, and N. H. Sleep (1981), Subduction zone calibration and teleseismic relocation of thrust zone events in the central Aleutian islands, *Bull. Seismol. Soc. Am.*, *71*, 1805–1828.

Fujiwara, S., P. Rosen, M. Tobita, and M. Murakami (1998), Crustal deformation measurements using repeat-pass JERS 1 synthetic aperture radar interferometry near the Izu Peninsula, Japan, *J. Geophys. Res.*, *103*, 2411–2426.

Hanssen, R. A. (2001), *Radar Interferometry: Data Interpretation and Error Analysis*, Springer, New York.

Hartzell, S. H., and C. Langer (1993), Importance of model parameterization in finite fault inversions: Application to the 1974 M_w 8.0 Peru earthquake, *J. Geophys. Res.*, *98*, 22,123–22,134.

Hartzell, S. H., P. Liu, and C. Mendoza (1996), The 1994 Northridge, California earthquake: Investigation of rupture velocity, rise time, and high-frequency radiation, *J. Geophys. Res.*, *101*, 20,091–20,108.

Hearn, E. H., R. Bürgmann, and R. E. Reilinger (2002), Dynamics of İzmit earthquake postseismic deformation and loading of the Düzce earthquake hypocenter, *Bull. Seismol. Soc. Am.*, *92*, 172–193.

Hernandez, B., F. Cotton, and M. Campillo (1999), Contribution of radar interferometry to a two-step inversion of the kinematic process of the 1992 Landers earthquake, *J. Geophys. Res.*, *104*, 13,083–13,099.

Husen, S., E. Kissling, E. Flueh, and G. Asch (1999), Accurate hypocentre determination in the seismogenic zone of the subducting Nazca Plate in northern Chile using a combined on-/offshore network, *Geophys. J. Int.*, *138*, 687–701.

Ihmlé, P. F., and R. Madariaga (1996), Monochromatic body waves excited by great subduction zone earthquakes, *Geophys. Res. Lett.*, *23*, 2999–3002.

Ihmlé, P. F., and J.-C. Ruegg (1997), Source tomography by simulated annealing using broad-band surface waves and geodetic data: Application to the $M_w = 8.1$ Chile 1995 event, *Geophys. J. Int.*, *131*, 146–158.

Ji, C., D. J. Wald, and D. V. Helmberger (2002a), Source description of the 1999 Hector Mine, California, earthquake, part I: Wavelet domain inversion theory and resolution analysis, *Bull. Seismol. Soc. Am.*, *92*, 1192–1207.

Ji, C., D. J. Wald, and D. V. Helmberger (2002b), Source description of the 1999 Hector Mine, California, earthquake, part II: Complexity of slip history, *Bull. Seismol. Soc. Am.*, *92*, 1208–1226.

Ji, C., D. V. Helmberger, D. J. Wald, and K. F. Ma (2003), Slip history and dynamic implications of the 1999 Chi-Chi, Taiwan, earthquake, *J. Geophys. Res.*, *108*(B9), 2412, doi:10.1029/2002JB001764.

Kanamori, H., and J. Given (1982), Use of long-period surface-waves for rapid-determination of earthquake source parameters: 2. Preliminary determination of source mechanisms of large earthquakes ($M_s > 6.5$) in 1980, *Phys. Earth Planet. Inter.*, *30*, 260–268.

Kaverina, A., D. Dreger, and E. Price (2002), The combined inversion of seismic and geodetic data for the source process of the 16 October 1999, M_w 7.1 Hector Mine, California, earthquake, *Bull. Seismol. Soc. Am.*, *92*, 1266–1280.

Klotz, J., et al. (1999), GPS-derived deformation of the central Andes including the 1995 Antofagasta $M_w = 8.0$ earthquake, *Pure Appl. Geophys.*, *154*, 709–730.

Lawton, J., C. Frohlich, H. Pulpan, and G. V. Latham (1982), Earthquake activity at the Kodiak continental shelf, Alaska, determined by land and ocean bottom seismograph networks, *Bull. Seismol. Soc. Am.*, *72*, 207–220.

Lohman, R. B., and M. Simons (2004), Locations of selected small earthquakes in the Zagros mountains, *Geochem. Geophys. Geosyst.*, *6*, Q03001, doi:10.1029/2004GC000849.

Maggi, A., J. A. Jackson, K. Priestley, and C. Baker (2000), A re-assessment of focal depth distributions in southern Iran, the Tien Shan and northern India: Do earthquakes really occur in the continental mantle?, *Geophys. J. Int.*, *143*, 629–661.

Melbourne, T., F. Webb, J. Stock, and C. Reigber (2002), Rapid postseismic transients in subduction zones from continuous GPS, *J. Geophys. Res.*, *107*(B10), 2241, doi:10.1029/2001JB000555.

Monfret, T., L. Dorbath, J. P. Caminade, M. Pardo, D. Comte, and L. Ponce (1995), The July 30, Antofagasta earthquake: An 'hypocritical' seismic event (abstract), *Eos Trans. AGU*, *76*(46), Fall Meet. Suppl., F427.

Oleskevich, D. A., R. D. Hyndman, and K. Wang (1999), The updip and downdip limits to great subduction earthquakes: Thermal and structural models of Cascadia, south Alaska, SW Japan, and Chile, *J. Geophys. Res.*, *104*, 14,965–14,991.

Ortlieb, L., S. Barrientos, and N. Guzman (1996), Coseismic coastal uplift and coralline algae record in northern Chile: The 1995 Antofagasta earthquake case, *Quat. Sci. Rev.*, *15*, 949–960.

Pacheco, J. F., L. R. Sykes, and C. H. Scholz (1993), Nature of seismic coupling along simple plate boundaries of the subduction type, *J. Geophys. Res.*, *98*, 14,133–14,159.

Patzig, R., S. Shapiro, G. Asch, P. Giese, and P. Wigger (2002), Seismogenic plane of the northern Andean subduction zone from aftershocks of the Antofagasta (Chile) 1995 earthquake, *Geophys. Res. Lett.*, *29*(8), 1264, doi:10.1029/2001GL013244.

Patzwahl, R., J. Mechie, A. Schulze, and P. Giese (1999), Two-dimensional velocity models of the Nazca plate subduction zone between 19.5°S and 25°S from wide-angle seismic measurements during the CINCA95 project, *J. Geophys. Res.*, *104*, 7293–7317.

Pritchard, M. E. (2003), Recent crustal deformation in west-central South America, Ph.D. thesis, Calif. Inst. of Technol., Pasadena. (Available at http://etd.caltech.edu/etd/available/etd-06022003-105512/)

Pritchard, M. E., and M. Simons (2004), An InSAR-based survey of volcanic deformation in the central Andes, *Geochem. Geophys. Geosyst.*, *5*, Q02002, doi:10.1029/2003GC000610.

Pritchard, M. E., and M. Simons (2006), An aseismic fault slip pulse in northern Chile and along-strike variations in seismogenic behavior, *J. Geophys. Res.*, *111*, B08405, doi:10.1029/2006JB004258.

Pritchard, M. E., M. Simons, P. Rosen, S. Hensley, and F. Webb (2002), Coseismic slip from the 1995 July 30 M_w = 8.1 Antofagasta, Chile, earthquake as constrained by InSAR and GPS observations, *Geophys. J. Int.*, *150*, 362–376.

Reigber, C., G. W. Michel, J. Klotz, and D. Angermann (1997), The Antofagasta 1995 earthquake: Crustal deformation pattern as observed by GPS and D-INSAR, in *Proceedings of Third ERS Symposium on Space at the Service of Our Environment, Florence, Italy*, pp. 507–513, Eur. Space Agency, Paris.

Rosen, P. A., S. Hensley, H. A. Zebker, F. H. Webb, and E. J. Fielding (1996), Surface deformation and coherence measurements of Kilauea Volcano, Hawaii, from SIR-C radar interferometry, *J. Geophys. Res.*, *101*, 23,109–23,125.

Rosen, P. A., S. Hensley, I. R. Joughin, F. K. Li, S. N. Madsen, E. Rodríguez, and R. M. Goldstein (2000), Synthetic aperture radar interferometry, *Proc. IEEE*, *88*, 333–382.

Rosen, P. A., S. Hensley, G. Peltzer, and M. Simons (2004), Updated Repeat Orbit Interferometry Package released, *Eos Trans. AGU*, *85*(5), 47.

Rothman, D. H. (1986), Automatic estimation of large residual statics corrections, *Geophysics*, *51*, 337–346.

Ruegg, J. C., et al. (1996), The M_w = 8.1 Antofagasta (north Chile) earthquake July 30, 1995: First results from teleseismic and geodetic data, *Geophys. Res. Lett.*, *23*, 917–920.

Ruff, L. J., and B. W. Tichelaar (1996), What controls the seismogenic plate interface in subduction zones?, in *Subduction: Top to Bottom, Geophys. Monogr. Ser.*, vol. 96, edited by G. E. Bebout et al., pp. 105–111, AGU, Washington, D. C.

Sagiya, T., and W. Thatcher (1999), Coseismic slip resolution along a plate boundary megathrust: The Nankai Trough, southwest Japan, *J. Geophys. Res.*, *104*, 1111–1129.

Salichon, J., B. Delouis, P. Lundgren, D. Giardini, M. Constantini, and P. Rosen (2003), Joint inversion of broadband teleseismic and interferometric synthetic aperture radar (InSAR) data for the slip history of the M_w = 7.7, Nazca Ridge (Peru) earthquake of 12 November 1996, *J. Geophys. Res.*, *108*(B2), 2085, doi:10.1029/2001JB000913.

Satake, K. (1993), Depth distribution of coseismic slip along the Nankai Trough, Japan, from joint inversion of geodetic and tsunami data, *J. Geophys. Res.*, *98*, 4553–4565.

Scharroo, R., P. N. A. M. Visser, and G. J. Mets (1998), Precise orbit determination and gravity field improvement for the ERS satellites, *J. Geophys. Res.*, *103*, 8113–8127.

Scholz, C. H. (1998), Earthquakes and friction laws, *Nature*, *391*, 37–42.

Segall, P., and J. L. Davis (1997), GPS applications for geodynamics and earthquake studies, *Annu. Rev. Earth Planet. Sci.*, *25*, 301–336.

Sen, M. K., and P. L. Stoffa (1995), *Global Optimization Methods in Geophysical Inversion*, Elsevier, New York.

Simons, M., Y. Fialko, and L. Rivera (2002), Coseismic deformation from the 1999 M_w 7.1 Hector Mine, California, earthquake as inferred from InSAR and GPS observations, *Bull. Seismol. Soc. Am.*, *92*, 1390–1402.

Suarez, G., and D. Comte (1993), Comment on "Seismic coupling along the Chilean subduction zone" by B. W. Tichelaar and L. R. Ruff, *J. Geophys. Res.*, *98*, 15,825–15,828.

Tichelaar, B. W., and L. J. Ruff (1991), Seismic coupling along the Chilean subduction zone, *J. Geophys. Res.*, *96*, 11,997–12,022.

Tichelaar, B. W., and L. J. Ruff (1993), Reply, *J. Geophys. Res.*, *98*, 15,829–15,831.

Wald, D. J., and R. W. Graves (2001), Resolution analysis of finite fault source inversion using one- and three-dimensional Green's functions: 2. Combining seismic and geodetic data, *J. Geophys. Res.*, *106*, 8767–8788.

Wald, D. J., and T. H. Heaton (1994), Spatial and temporal distribution of slip for the 1992 Landers, California, earthquake, *Bull. Seismol. Soc. Am.*, *84*, 668–691.

Wald, D. J., T. H. Heaton, and K. W. Hudnut (1996), The slip history of the 1994 Northridge, California, earthquake determined from strong-motion, teleseismic, GPS, and leveling data, *Bull. Seismol. Soc. Am.*, *86*, S49–S70.

Wessel, P., and W. H. F. Smith (1998), New, improved version of Generic Mapping Tools released, *Eos*, *79*, 579.

Xia, Y., G. W. Michel, C. Riegber, J. Klotz, and H. Kaufmann (2003), Seismic unloading and loading in northern central Chile as observed by differential synthetic aperture radar interferometry (D-INSAR) and GPS, *Int. J. Remote Sens.*, *24*, 4375–4391.

Zebker, H. A., P. A. Rosen, R. M. Goldstein, A. Gabriel, and C. L. Werner (1994), On the derivation of coseismic displacement–fields using differential radar interferometry: The Landers earthquake, *J. Geophys. Res.*, *99*, 19,617–19,634.

————————————

C. Ji, Seismological Laboratory, Division of Geological and Planetary Sciences, California Institute of Technology, MC 252-21, Pasadena, CA 91125, USA.

M. E. Pritchard, Department of Earth and Atmospheric Sciences, Snee Hall, Cornell University, Ithaca, NY 14853, USA. (mp337@cornell.edu)

M. Simons, Department of Geological Sciences, University of California, Santa Barbara, CA 93106, USA.